CORA Cork Open Research Archive
Cartlann Taighde Oscailte Chorcaí

Title	Vortex-induced chaotic mixing in wavy channels
Authors	Lee, Wei-Koon;Taylor, P. H.;Borthwick, Alistair G. L.;Chuenkum, S.
Publication date	2010-07-10
Original Citation	WEI-KOON LEE, P. H. TAYLOR, A. G. L. BORTHWICK and S. CHUENKHUM (2010). Vortex-induced chaotic mixing in wavy channels. Journal of Fluid Mechanics, 654 , pp 501-538 doi:10.1017/S0022112010000674
Type of publication	Article (peer-reviewed)
Link to publisher's version	10.1017/S0022112010000674
Rights	© Cambridge University Press 2010
Download date	2026-10-15 01:41:13
Item downloaded from	https://hdl.handle.net/10468/484

UCC
University College Cork, Ireland
Coláiste na hOllscoile Corcaigh

J. Fluid Mech. (2010), *vol.* 654, *pp.* 501–538. © Cambridge University Press 2010
doi:10.1017/S0022112010000674

Vortex-induced chaotic mixing in wavy channels

WEI-KOON LEE†, P. H. TAYLOR, A. G. L. BORTHWICK AND S. CHUENKHUM

Department of Engineering Science, University of Oxford, Parks Road, Oxford OX1 3PJ, UK

(Received 14 May 2009; revised 11 January 2010; accepted 2 February 2010; first published online 11 May 2010)

Mixing is studied in open-flow channels with conformally mapped wavy-wall profiles, using a point-vortex model in two-dimensional irrotational, incompressible mean flow. Unsteady dynamics of the separation bubble induced by oscillatory motion of point vortices located in the trough region produces chaotic mixing in the Lagrangian sense. Significant mass exchange between passive tracer particles inside and outside of the separation bubble forms an efficient mixing region which evolves in size as the vortex moves in the unsteady potential flow. The dynamics closely resembles that obtained by previous authors from numerical solutions of the unsteady Navier–Stokes equations for oscillatory unidirectional flow in a wavy channel. Of the wavy channels considered, the skew-symmetric form is most efficient at promoting passive mixing. Diffusion via gridless random walks increases lateral particle dispersion significantly at the expense of longitudinal particle dispersion due to the opposing effect of mass exchange at the front and rear of the particle ensemble. Active mixing in the wavy channel reveals that the fractal nature of the unstable manifold plays a crucial role in singular enhancement of productivity. Hyperbolic dynamics dominate over non-hyperbolicity which is restricted to the vortex core region. The model is simple yet qualitatively accurate, making it a potential candidate for the study of a wide range of vortex-induced transport and mixing problems.

1. Introduction

The phenomenon of Lagrangian chaos has been a subject of great interest following the landmark demonstration by Aref (1984) of chaotic particle motion beyond that of the underlying fluid dynamics. Using what is now known as the blinking-vortex model, Aref (1984) reported complex particle motion induced by the time-periodic agitation of a pair of point vortices in an idealized two-dimensional closed fluid system. The enhancement of mixing in relatively simple Eulerian unsteady flows has since been extensively researched. Chaotic motion, or chaos in general, is characterized by sensitivity to initial conditions, aperiodic motion with rapid divergence and unpredictability despite being deterministic. Ottino (1989) gave a detailed account of mixing and chaos and described the many analytical tools developed in the field of nonlinear dynamics, which underwent rapid progress in the 1980s.

The transport and mixing problem in a wavy channel can be characterized by a relatively simple flow field but intrinsically complex chaotic particle motions due to vortical stirring. Hence, unless the flow is fully turbulent, a point-vortex model involving few

† Email address for correspondence: wei.lee@eng.ox.ac.uk

degrees of freedom can be a particularly attractive way to give a simple and concise description of the flow field which is dominated by vortex-induced circulation.

Rom-Kedar, Leonard & Wiggins (1990) examined transport and mixing in a two-dimensional inviscid incompressible flow governed by an oscillating vortex pair. They studied the global topology of chaotic particle motions for small perturbations of an external strain-rate field that caused the vortex pair to oscillate about its equilibrium position. For the perturbed flow, the invariant stable and unstable manifolds, defined as the sets of all phase space points from which particles can reach the hyperbolic fixed point in forward and reversed time respectively (Tél & Gruiz 2006), are shown to intersect each other transversely, resulting in tangled flow structures which are responsible for fluid transport in the mixing region. The dynamics of the unsteady vortical flow reported by Rom-Kedar *et al.* (1990) approximates the study of flows in furrowed channels with wavy-wall profiles and time-periodic volumetric flow rates considered by Sobey (1980). The flow field in the vicinity of the oscillating vortex pair corresponds to the instant when the vortex formed from flow separation is ejected into the main stream, with recirculating flow between the vortex and the wall. It is thus limited to the case in which the oscillating vortex pair is sufficiently distant from the wall. In the present work, we extend the above study to consider the effects when the vortices move in relatively large orbits such that they interact with the wall via image vortices. We consider mixing of an inviscid flow in furrowed open-flow devices characterized by a wavy-wall profile previously described by Taylor (1981). The flow field comprises a uniform mean flow and self-sustaining point vortices in the furrows. Strong mixing cases are considered where the circulations induced by the point vortices dominate over other processes such as boundary effects at the wall. Our primary interest is to investigate the particle convection. Using a simple approximation, both the vortices and particles are assumed to take on the velocity of the resulting flow field and are tracked using a Lagrangian technique. Since the study involves only kinematical considerations, the model is independent of Reynolds number but should apply to a real laminar flow subjected to external stirring actions such as in the blinking-vortex experiments (Aref 1984). Analysis of particle motion in such flows from a Lagrangian point of view is very similar to that of flow visualization techniques. We show that our point-vortex model reproduces some of the salient features of mixing in a wavy channel similar to that obtained from numerical solution of the Navier–Stokes equations (Sobey 1980). In addition, several observations unique to the present model are presented and discussed.

We note that flow over wavy boundaries is a generic problem in fluid mechanics. It is important in the generation and growth of waves in the open ocean, where the rapid growth of short steep waves is largely due to flow separation at their sharp crests (see e.g. Csanady 2001). It is also of direct relevance in the modelling of 'singing pipes', where high-speed gas or liquid flow in corrugated pipes can excite acoustic organ-pipe modes (e.g. Crawford 1974; Silverman & Cushman 1989; Cadwell 1994; see also the discussions by Walker 2007, § 3.39). In each of these problems, a simple point-vortex potential flow model could be useful for exploring some of the important physical processes. In the present paper, we concentrate on mixing induced by unsteady vortex motion. In contrast, for aero-acoustic problems such as the singing pipe, the unsteady vortex motion itself is responsible for driving and responding to the acoustic modes (Howe 2003).

Numerical simulation (Sobey 1980) and experimental observations (Stephanoff, Sobey & Bellhouse 1980) of flows in furrowed channels have revealed that flow separation occurs in the hollows at Reynolds numbers above a threshold value. For

unsteady flow, deceleration of fluid in the diverging part of the channel leads to the cyclic formation, growth, ejection and decay of vortices which enhance convective mixing. This behaviour has allowed the design of devices capable of efficient mixing and mass transfer in an open system in the absence of turbulence, such as membrane oxygenators. Sobey (1982) made similar observations for flows in wavy channels with asymmetric geometry. Sobey (1985) further studied the occurrence of Lagrangian convective dispersion caused by unsteady separation during oscillatory flow through a furrowed channel in the absence of Brownian diffusion and demonstrated that the variance of fluid particles grows approximately linearly with time.

Using a numerical scheme similar to that of Sobey (1980), Ralph (1986) presented results for viscous oscillatory flow in wavy-walled tubes with the aid of flow visualization. At large Strouhal number, the flow structure is similar to that obtained by Sobey (1980) at low Reynolds number but high enough that separation occurs. Development of time-asymmetric flows in a limited region of the parameter space may be regarded as a bifurcation of the flow structure and is suggestive of transition to turbulence, analogous to a forced nonlinear oscillator from the viewpoint of a dynamical system (Roberts & Mackley 1996). In a study of self-sustaining oscillatory flows in a converging-diverging channel, Guzmán & Amon (1994) showed that the transition from laminar to chaotic flow occurs via a series of Hopf bifurcations as the Reynolds number is increased, consistent with the Ruelle–Takens–Newhouse scenario of the onset of chaos. Chaotic particle trajectories have been verified and analysed using measures such as fractal dimensions and Lyapunov exponents (Amon, Guzmán & Morel 1996; Guzmán & Amon 1996).

The paper is organized as follows: § 2 presents the derivation of the equations of motion for the vortex and passive particles in three different configurations, namely the wavy-wall problem, the symmetrical channel and the skew-symmetrical channel. Section 3 describes briefly the numerical solver. Section 4 examines the vortex motion, analytically and numerically. We show that the vortices move in regular trajectories with negligible influence from the neighbouring vortices. Section 5 looks at the presence of Lagrangian chaos in all three configurations under the stirring action of the vortices. Section 6 shows that chaotic mixing is primarily induced by the unsteady dynamics of the separation bubbles which move and evolve in size with the vortices at all times. The vortex core, free-flow region and mixing region in the flow field are identified. We show that the dynamics are related to an oscillatory unidirectional flow of a real fluid described by Sobey (1980). The structures of the stable and unstable manifolds are presented, and their role in the mixing process is discussed. Section 7 investigates the efficiencies of passive mixing in the three configurations. The effect of Brownian diffusion is found to increase lateral particle dispersion at the expense of longitudinal particle dispersion. Section 8 considers autocatalytic reaction in the wavy channel and the fractal form of the unstable manifold. Conclusions are listed in § 9.

2. Equations of motion

Two-dimensional irrotational, incompressible fluid flow is considered. The stream function automatically satisfies the continuity equation, and the velocity potential exists everywhere in the fluid except at singularities.

2.1. *Flow over a wavy wall*

Consider a uniform flow field of velocity U in the x-direction over a flat wall located at $y = 0$. A point vortex which is rotating clockwise in the flow field has strength of

$-\kappa$, and the actual circulation is $-2\pi\kappa$. Using the method of images (Milne-Thomson 1968), the complex potential function is given by

$$w(z) = Uz + \mathrm{i}\kappa \log((z - \bar{z}_v)/(z - z_v)), \tag{2.1}$$

where z_v is the vortex position, and the overbar indicates the complex conjugate. The flow regime is bounded by the wall ($y \geqslant 0$), and the complex velocity is

$$\frac{\mathrm{d}w}{\mathrm{d}z} = U + \mathrm{i}\kappa \left[\frac{1}{z - \bar{z}_v} - \frac{1}{z - z_v}\right]. \tag{2.2}$$

A conformal transformation that maps the flat wall in the z-plane on to a wavy wall in the ζ-plane is given as

$$\zeta = f(z) = z + \mathrm{i}\epsilon \exp(\mathrm{i}Kz), \tag{2.3}$$

where the constants ϵ and K are the amplitude and the wavenumber of the wall respectively (Taylor 1981). To satisfy the smooth-wall condition and ensure the existence of a conformal transformation for the fluid region, the constants are restricted such that $\epsilon K \leqslant 1$. The complex velocity at any point in the ζ-plane can be calculated using the chain rule,

$$\frac{\mathrm{d}W}{\mathrm{d}\zeta} = \frac{\mathrm{d}w}{\mathrm{d}z}\frac{\mathrm{d}z}{\mathrm{d}\zeta} = \frac{\mathrm{d}w}{\mathrm{d}z}\frac{1}{f'(z)} = u_\xi - \mathrm{i}v_\eta. \tag{2.4}$$

Equation (2.4) shows that the complex velocities are not mapped one to one but are proportional depending on the mapping functions. Although the transformation function $\zeta = f(z)$ can be chosen to be a simple analytic function, solution of the inverse transformation $z = f^{-1}(\zeta)$ will require numerical iteration. To avoid this, the vortex position in the ζ-plane is expressed in the form of $\zeta(z) = \xi(x, y) + \mathrm{i}\eta(x, y)$. Taking the time derivative, followed by the complex conjugate, the motion of passive particles when tracked in the z-plane can thus be written as

$$\frac{\mathrm{d}\bar{z}}{\mathrm{d}t} = \frac{1}{|f'(z)|^2}\frac{\mathrm{d}w}{\mathrm{d}z}. \tag{2.5}$$

A direct transformation using (2.3) will then give the particle trajectories in the physical domain in the ζ-plane but followed in the z-plane.

For vortex tracking, Routh (1881) introduced a correction term to account for the fact that the transformation of the vortex path in one plane is not the path in the new plane. Thus, the vortex motion in terms of its position in the z-plane is

$$\frac{\mathrm{d}\bar{z}_v}{\mathrm{d}t} = \frac{1}{|f'(z_v)|^2}\left\{U + \mathrm{i}\kappa\left[\frac{1}{z_v - \bar{z}_v} + \frac{f''(z_v)}{2f'(z_v)}\right]\right\}. \tag{2.6}$$

Equation (2.2) can be extended to represent a row of $2N + 1$ vortices which are in phase and of equal strength, with one vortex spaced every wavelength λ ($= 2\pi/K$) along the wall, within the uniform flow field of velocity U (figure 1), giving

$$w(z) = Uz + \mathrm{i}\kappa \sum_{n=-N}^{N} \log\left[\frac{(z - \bar{z}_v) + n\lambda}{(z - z_v) + n\lambda}\right], \tag{2.7}$$

where the coordinates of the vortex array in the z-plane are $(x_v \pm n\lambda, y_v)$, $n = 0, 1, \ldots, N$. The equations of motion for passive particles and the vortex ($z = z_v$) are

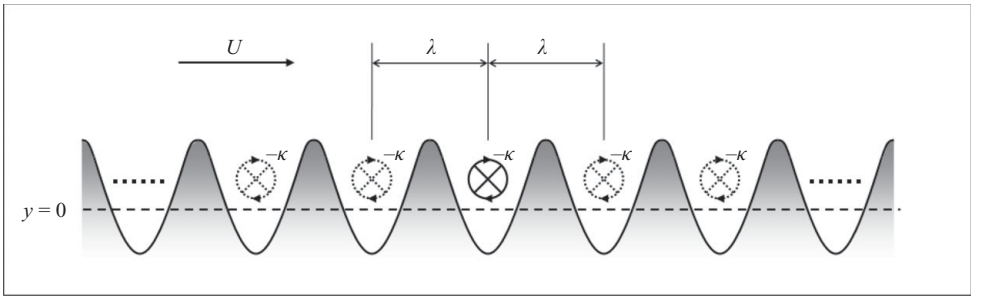

FIGURE 1. Wavy-wall problem with an array of vortices.

thus

$$\frac{\mathrm{d}\bar{z}}{\mathrm{d}t} = \frac{1}{|f'(z)|^2}\left\{U + \mathrm{i}\kappa \sum_{n=-N}^{N}\left[\frac{1}{z-\bar{z}_v+n\lambda} - \frac{1}{z-z_v+n\lambda}\right]\right\} \tag{2.8}$$

and

$$\frac{\mathrm{d}\bar{z}_v}{\mathrm{d}t} = \frac{1}{|f'(z_v)|^2}\left\{U + \mathrm{i}\kappa \left[\sum_{n=-N}^{N}\left(\frac{1}{z-\bar{z}_v+n\lambda}\right) + \frac{f''(z_v)}{2f'(z_v)}\right]\right\} \tag{2.9}$$

respectively.

Considering a system with an infinite number of vortices such that $N = \infty$, the summation term in (2.8) and (2.9) can be written as

$$\sum_{-\infty}^{\infty}\frac{1}{z-\bar{z}_v+n\lambda} = \sum_{-\infty}^{\infty}\frac{z-\bar{z}_v}{(z-\bar{z}_v)^2+n^2(\mathrm{i}\lambda)^2}. \tag{2.10}$$

Following Lamb (1953), we have

$$\frac{k}{2\pi}\sum_{-\infty}^{\infty}\frac{b}{b^2+n^2a^2} = \frac{k}{2a}\coth\frac{\pi b}{a}. \tag{2.11}$$

Equations (2.8) and (2.9) thus become

$$\frac{\mathrm{d}\bar{z}}{\mathrm{d}t} = \frac{1}{|f'(z)|^2}\left\{U + \mathrm{i}\kappa\left[\frac{K}{2\mathrm{i}}\coth\frac{K(z-\bar{z}_v)}{2\mathrm{i}} - \frac{K}{2\mathrm{i}}\coth\frac{K(z-z_v)}{2\mathrm{i}}\right]\right\} \tag{2.12}$$

and

$$\frac{\mathrm{d}\bar{z}_v}{\mathrm{d}t} = \frac{1}{|f'(z_v)|^2}\left\{U + \mathrm{i}\kappa\left[\frac{K}{2\mathrm{i}}\coth y_v K + \frac{f''(z_v)}{2f'(z_v)}\right]\right\} \tag{2.13}$$

respectively.

2.2. *Flow in a symmetrical wavy channel*

We consider a channel of uniform width 2π where the walls are located at $y = \pm\mathrm{i}\pi$ in the z-plane, and the flow field comprises a uniform velocity of U and a pair of point vortices, one of strength κ located at $z = z_v$ and the other of strength $-\kappa$ located at $z = \bar{z}_v$. Using the method of images as before, the above problem becomes one of an infinite number of vortex pairs in the y-direction. At an arbitrary point of interest z, the complex velocity can be expressed as

$$\frac{\mathrm{d}w}{\mathrm{d}z} = U + \mathrm{i}\kappa\sum_{n=-\infty}^{\infty}\left[\frac{1}{z-z_v+\mathrm{i}2n\pi} - \frac{1}{z-\bar{z}_v+\mathrm{i}2n\pi}\right]. \tag{2.14}$$

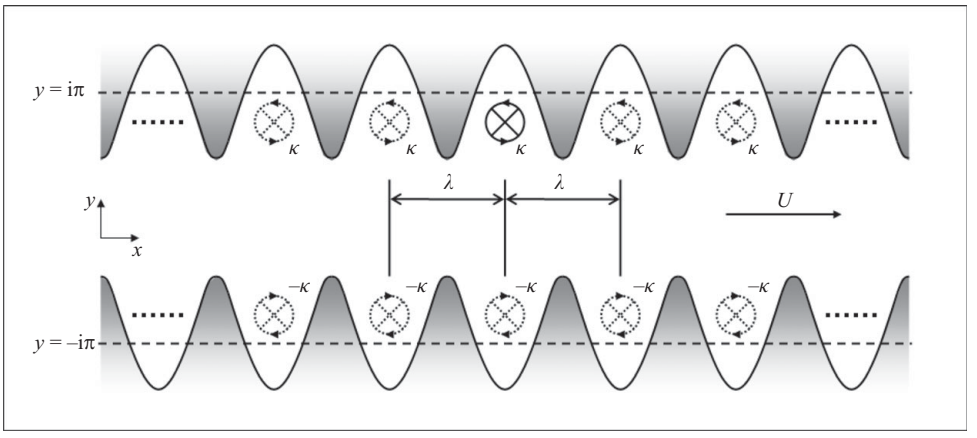

FIGURE 2. Symmetrical wavy channel with an array of vortices.

Rewriting the summation term as in the preceding section followed by integration, the complex potential function of the flow system is thus

$$w(z) = Uz + \mathrm{i}\kappa \log \frac{\sin \mathrm{i}(z - \overline{z}_v)/2}{\sin \mathrm{i}(z - z_v)/2}, \tag{2.15}$$

as obtained previously by Cannell & Ffowcs Williams (1973).

The uniform width channel in the z-plane above is conformally mapped to a symmetrical wavy channel in the ζ-plane, using the mapping function

$$\zeta = f(z) = z + \mathrm{i}\epsilon[\exp(\mathrm{i}Kz) - \exp(-\mathrm{i}Kz)], \tag{2.16}$$

where K again is the wavenumber. However, ϵ is no longer the amplitude of the wave on the wall but is simply proportional to it (Taylor 1981).

Consider $2N + 1$ pairs of in-phase vortices of equal but opposite strength in the symmetrical wavy channel, with one vortex per wavelength of the wall, within the uniform flow field of velocity U (figure 2), where the coordinates of the vortex array in the z-plane are $(x_v \pm n\lambda, \pm y_v)$, $n = 0, 1, \ldots, N$. Following the derivation presented in § 2.1, the motion of passive particles tracked in the z-plane is thus

$$\frac{\mathrm{d}\overline{z}}{\mathrm{d}t} = \frac{1}{|f'(z)|^2} \left\{ U + \frac{\kappa}{2} \sum_{n=-N}^{N} \left[\cot \frac{\mathrm{i}}{2}(z - z_v + n\lambda) - \cot \frac{\mathrm{i}}{2}(z - \overline{z}_v + n\lambda) \right] \right\}. \tag{2.17}$$

For vortex tracking, the correction term owing to Routh (1881) is introduced as before, giving

$$\frac{\mathrm{d}\overline{z}_v}{\mathrm{d}t} = \frac{1}{|f'(z_v)|^2} \left\{ U + \mathrm{i}\kappa \sum_{n=-N}^{N} \left[-\frac{1}{2\mathrm{i}} \cot \frac{\mathrm{i}}{2}(z_v - \overline{z}_v + n\lambda) \right] + \frac{f''(z_v)}{2f'(z_v)} \right\}. \tag{2.18}$$

2.3. *Flow in a skew-symmetrical wavy channel*

Consider a channel of uniform width 2π where the walls are located at $y = 0$ and $y = \mathrm{i}2\pi$ respectively in the z-plane. The flow field comprises a uniform velocity U and a pair of point vortices, one with strength κ located at $z = z_v$ and another with strength $-\kappa$ located at $z = c_v = (\overline{z}_v + \lambda/2) + \mathrm{i}2\pi$. Using the method of images (figure 3), we first consider the infinite number of vortices in the y-direction. The

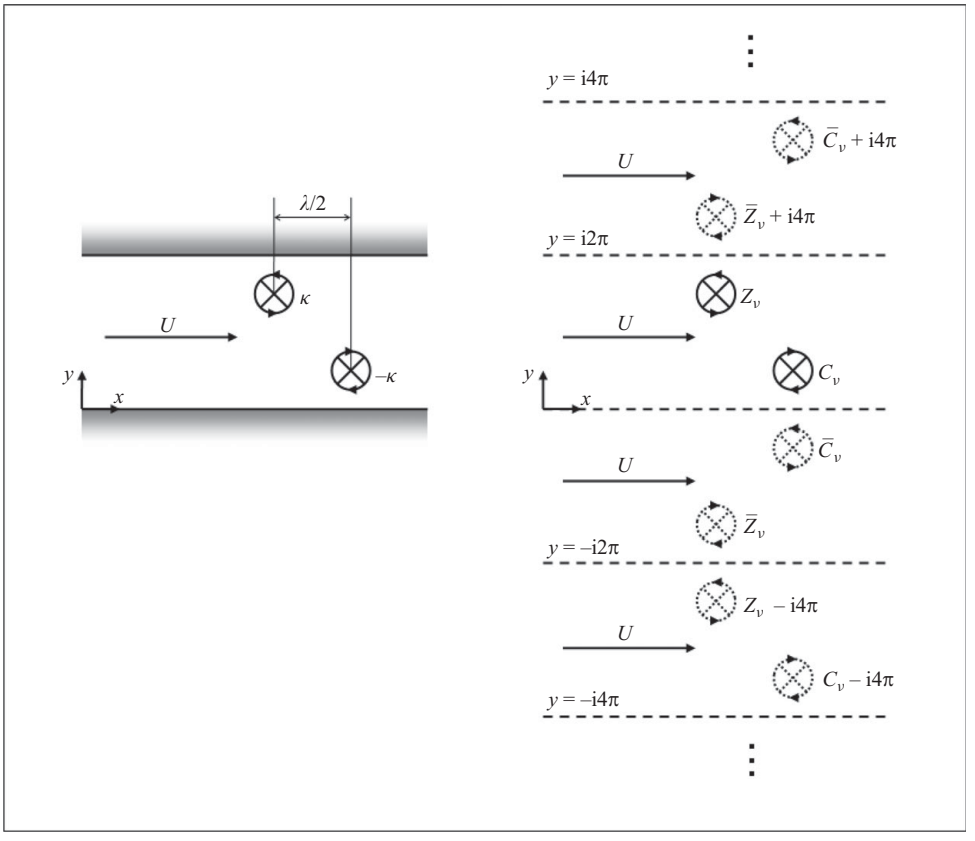

FIGURE 3. Method of images for skew-symmetrical wavy channel.

complex velocity at a point of interest z can be written as

$$\frac{\mathrm{d}w}{\mathrm{d}z} = U + \mathrm{i}\kappa \sum_{n=-\infty}^{\infty} \left[\frac{1}{z - z_v + \mathrm{i}4n\pi} - \frac{1}{z - \bar{z}_v + \mathrm{i}4n\pi} + \frac{1}{z - \bar{c}_v + \mathrm{i}4n\pi} - \frac{1}{z - c_v + \mathrm{i}4n\pi} \right], \tag{2.19}$$

where the infinite summation term can be treated as in § 2.1.

Next, we consider $2N + 1$ ($-N$ to N) vortices along the upper wall and a corresponding $2N$ ($-N$ to $N-1$) vortices along the lower wall such that symmetry is maintained in the longitudinal direction (figure 4). Incorporating this into (2.19), we get

$$\frac{\mathrm{d}w}{\mathrm{d}z} = U + \mathrm{i}\kappa \sum_{n=-N}^{N} M, \tag{2.20}$$

where

$$M = \frac{1}{4\mathrm{i}} \left[\cot \frac{\mathrm{i}(z - Z_v)}{4} - \cot \frac{\mathrm{i}(z - \overline{Z}_v)}{4} + \cot \frac{\mathrm{i}(z - \overline{C}_v)}{4} - \cot \frac{\mathrm{i}(z - C_v)}{4} \right] \tag{2.21}$$

and $Z_v = z_v + n\lambda$, $C_v = [\bar{z}_v + \lambda(2n + 1)/2] + \mathrm{i}2\pi$.

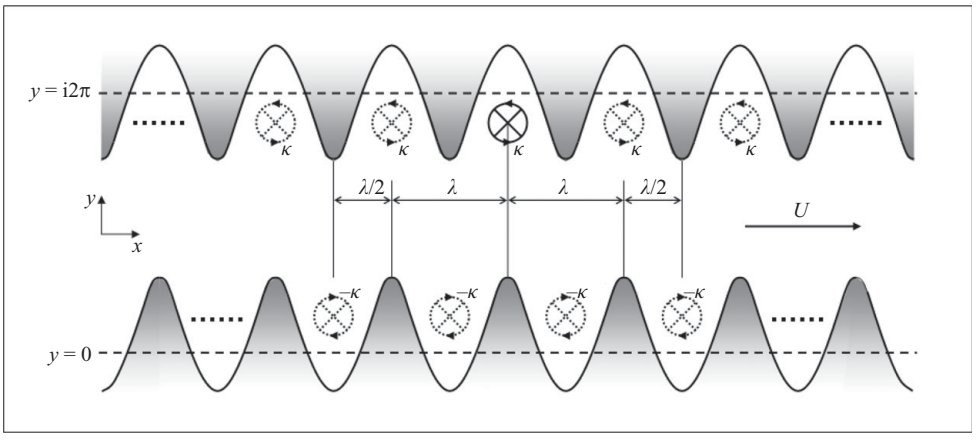

FIGURE 4. Skew-symmetrical wavy channel with an array of vortices.

The motion of passive particles and vortices tracked in the z-plane can be described by

$$\frac{\mathrm{d}\overline{z}}{\mathrm{d}t} = \frac{1}{|f'(z)|^2}\left\{U + \mathrm{i}\kappa \sum_{n=-N}^{N} M\right\} \tag{2.22}$$

and

$$\frac{\mathrm{d}\overline{z}_v}{\mathrm{d}t} = \frac{1}{|f'(z_v)|^2}\left\{U + \mathrm{i}\kappa\left[\sum_{n=-N}^{N}\left(-\frac{\cot \mathrm{i}(z_v - \overline{Z}_v)/4}{4\mathrm{i}} - \frac{\cot \mathrm{i}(z_v - C_v)/4}{4\mathrm{i}}\right) + \frac{f''(z_v)}{2f'(z_v)}\right]\right\} \tag{2.23}$$

respectively, where the mapping function used to transform the uniform channel into a skew-symmetrical wavy channel is

$$\zeta = f(z) = z + \mathrm{i}\epsilon[\exp(\mathrm{i}K(z - \mathrm{i}\pi)) + \exp(-\mathrm{i}K(z - \mathrm{i}\pi))]. \tag{2.24}$$

3. Numerical solution of the flow model

The wall wavelength λ is chosen as the characteristic length L_0 to non-dimensionalize the length scales, giving $\tilde{x} = x/L_0$, $\tilde{y} = y/L_0$, $\tilde{\xi} = \xi/L_0$ and $\tilde{\eta} = \eta/L_0$. Letting the mean incoming velocity U_0 be the characteristic velocity, the dimensionless velocity, vortex strength and time are thus given by $\tilde{U} = U/U_0$, $\tilde{\kappa} = \kappa/U_0L_0$ and $\tilde{t} = U_0t/L_0$ respectively. Two dimensionless parameters are defined herein, namely the dimensionless amplitude of vortex motion Λ $(= \Delta\xi/\lambda)$ and the Strouhal number Ω $(= \lambda/UT)$, where T is the period of the resonance. The classical fourth-order Runge–Kutta scheme is adopted to solve the equations of motion in the z-plane. A time step Δt of 0.01 gives stable, converged solutions and is used throughout, unless otherwise stated. All figures are plotted using the dimensionless quantities, and the tildes are dropped for convenience.

4. Vortex motion in vicinity of wavy wall

4.1. *Perturbation analysis of vortex motion*

For the wavy-wall problem (§ 2.1), the equilibrium position of the vortex is taken to be in the middle of the wall corrugation such that $\xi_e = \pi$ and $\eta_e = 0$. Solving the mapping

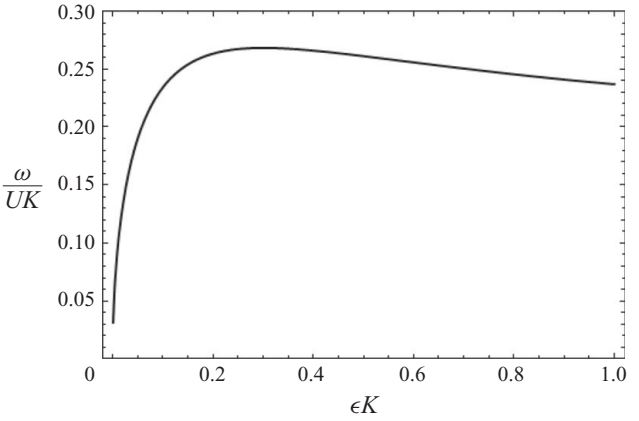

FIGURE 5. Strouhal number of vortex as a function of ϵK.

function (2.3) then yields the corresponding position in the computational domain given by $x_e = \pi$ and an inverse function $y_e \exp(y_e) = \epsilon$. Defining the vortex position as $z_v = x_v + \mathrm{i}y_v = (x_e + X) + \mathrm{i}(y_e + Y)$, where X and Y are small perturbations from the equilibrium position in the z-plane, the case of a single vortex ($N = 0$) as described by (2.6) can then be written as

$$\frac{\mathrm{d}\bar{z}_v}{\mathrm{d}t} = \dot{X} - \mathrm{i}\dot{Y}, \tag{4.1}$$

where the dot indicates time derivative. For a stationary vortex, the equilibrium vortex strength can thus be expressed as

$$\kappa_e = \frac{-2U(\epsilon + \exp y_e)}{-\epsilon + \exp y_e \coth y_e + \epsilon \coth y_e}. \tag{4.2}$$

Setting the wavy-wall parameters $\epsilon = 0.5$ and $K = 1$ after Taylor (1981), the above formulations give $y_e \approx 0.3517$ and $\kappa_e \approx -0.7743U$. Adopting unit uniform flow ($U = 1$) throughout and $\kappa = \kappa_e$, different degrees of mixing, characterized by the amplitude of vortex motion Λ, can thus be selected by defining only the initial vortex position (x_{v0}, y_{v0}). For convenience, we choose $x_{v0} = x_e$ (i.e. $X = 0$) such that the initial vortex position is always in the middle of the trough, and the sole parameter that remains to be specified is the perturbation term Y where $y_{v0} = y_e + Y$.

We note that the equilibrium vortex strength reduces monotonically with decreasing value of ϵ, which represents the wall waviness for $K = 1$. In an experimental study of vortices in wavy profiles, Wierschem, Scholle & Aksel (2003) reported increasing critical flow thickness for vortex formation at reduced wall waviness. In their experiment, the vortex formed is essentially stationary and symmetrical because of steady gravity-driven flow. Hence, except in the limit in which ϵ vanishes, our analytical equilibrium vortex strength in the middle of the furrow is analogous to weak to strong vortical motion as wall waviness increases.

Writing the linear approximation of the single-vortex motion in the form of $\dot{X} = a_1 Y$ and $\dot{Y} = a_2 X$, the coefficients a_1 and a_2 are readily determined. The angular frequency of the vortex motion, $\omega = 2\pi f = \sqrt{a_1 a_2}$, is thus a function of ϵ. Figure 5 shows the Strouhal number ω/UK $(= \lambda/UT)$ as a function of ϵK. The Strouhal number is only weakly dependent on ϵK, reducing from a maximum of 0.27 when $\epsilon K \approx 0.3$ to slightly below 0.24 when $\epsilon K \to 1$. The reversed and stronger form for $\epsilon K < 0.3$ is of

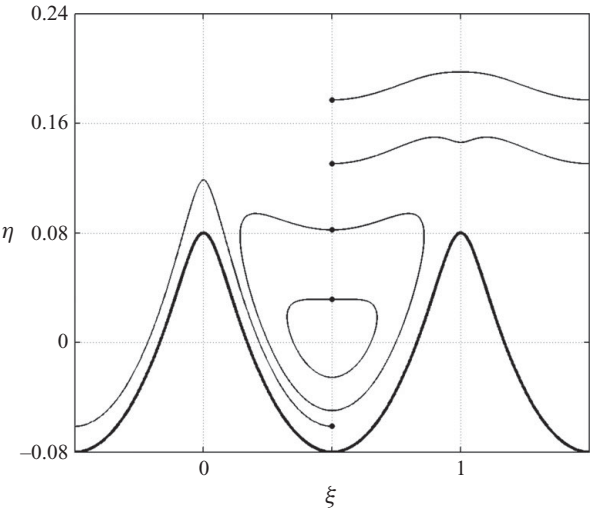

FIGURE 6. Single-vortex motion along the wavy wall: ●, initial position; ——, vortex trajectories.

little interest, as the small wall amplitude is unlikely to produce good mixing (Ottino 1989). In particular for $\epsilon K = 0.5$, the fundamental Strouhal number of a vortex is given by $\omega = 0.2611$.

Writing the solution of the linear approximation in the form of an undamped sinusoidal wave as a function of time t, we define $X = A \sin \omega t$ and $Y = -\alpha A \cos \omega t$, where α is a scaling factor which relates the amplitude of the vortex motion in the y-direction to that in the x-direction such that $0 < |\alpha| < 1$, and A is the dimensionless amplitude of motion in the x-direction. Substituting into the linear approximation and solving yields $\alpha = -0.1562$.

Solving (4.1) to a third-order approximation, two resonant terms of the fundamental Strouhal number arise because of the nonlinearity of the frequency of response (Nayfeh 1985). A correction term of the order of A^2 is applied to the Strouhal number and the scaling factor respectively, giving

$$\omega = \omega_0 + c_1 A^2, \quad \alpha = \alpha_0 + c_2 A^2, \tag{4.3a, b}$$

where $\omega_0 = 0.2611$ and $\alpha_0 = -0.1562$ as previously determined. Substituting ω and α into the modified linear approximation equations and solving, the coefficients c_1 and c_2 are obtained as 0.0266 and −0.0095 respectively. The complete solution to the third-order approximation of the vortex motion is thus given by

$$X = A \sin \omega t - 0.1107 A^2 \sin 2\omega t - 0.0035 A^3 \sin 3\omega t, \tag{4.4a}$$

$$Y = 0.0320 A^2 - \alpha A \cos \omega t - 0.0084 A^2 \cos 2\omega t - 0.0032 A^3 \cos 3\omega t. \tag{4.4b}$$

Using the same approach, a perturbation analysis for the $N = \infty$ case was performed and resulted in similar expressions for the Strouhal number and the scaling factor.

4.2. *Vortex path in a wavy trough*

Figure 6 shows the path taken by a single vortex when released from five different initial positions. If the vortex is too close to the wall, the coupling effect with its image has a dominant influence, causing the vortex to move upstream along the wall. On the other hand, if the vortex is too far away from the wall, the uniform flow effect

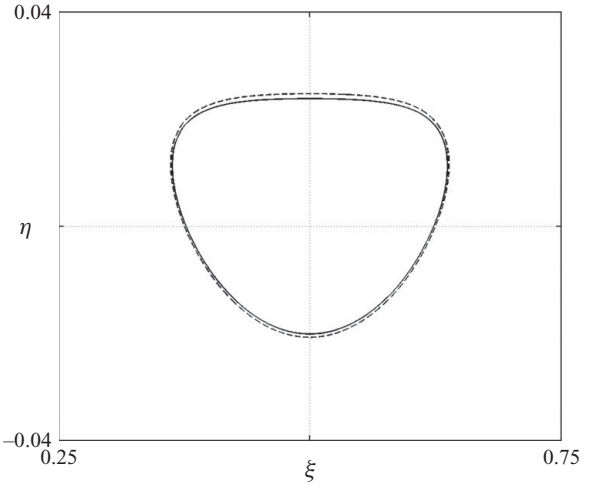

FIGURE 7. Comparison of vortex path derived from perturbation analysis (– – – –) and numerical iteration (——): $N = 0$, $z_v = (\pi, 0.260)$, $Y = -0.09$.

sweeps the vortex downstream, tracing the wall topography. Generally, if both κ and U are positive or negative, then the vortex will be swept downstream or upstream respectively by the uniform flow regardless of initial position. If $U = 0$, the vortex will couple with its image to form a simple vortex pair which advances at a velocity of $\kappa/2d$ along the x-direction, where d is the distance of the vortices from the wall. Our interest lies mainly with vortices located in the vicinity of the wall trough where the opposing flow effect from their respective images and the uniform flow field causes the vortices to be trapped in hydrodynamic oscillations.

Figure 7 compares the analytical vortex paths ($N = 0$) derived in § 4.1 with those obtained numerically from Lagrangian tracking. A small time step of $\Delta t = 0.001$ is adopted to simulate accurately the vortex motion. It can be seen that analytical results obtained from the perturbation analysis are in good agreement with the numerical predictions for small perturbation $|Y| \ll 0.09$ ($A \ll 0.2061$).

4.3. *Frequency–amplitude correlation*

Figure 8 plots the Strouhal number Ω versus the dimensionless amplitude Λ for wavy-wall cases with a single vortex ($N = 0$) and an infinite number of vortices ($N = \infty$). The solid curves give the frequency–amplitude correlation calculated numerically for different perturbations of initial vortex position, whereas the dashed curves plot the analytical frequency–amplitude correlation as described by (4.3*a*) where the equivalent dimensionless forms may be written as $\Omega = \omega/UK$ and $\Lambda = A = \Delta x/\lambda$. From the numerical solutions, we can see that Ω increases slowly with respect to Λ but shows an abrupt drop as Λ approaches the wavelength of the wall. This corresponds to lateral vortex motion beyond the wall crest level which approaches the point of escape from the influence of its image. The Strouhal number of the vortex array is slightly lower than the case of a single vortex. For linear perturbation away from the equilibrium position ($\Lambda = 0$), Ω equals 0.2611 and 0.2477 for the cases $N = 0$ and $N = \infty$ respectively, which agree well with the analytical results in § 4.1. The third-order analytical approximation gives an excellent approximation of the frequency–amplitude correlation for perturbation up to $\Lambda \sim 0.5$ for both $N = 0$ and $N = \infty$.

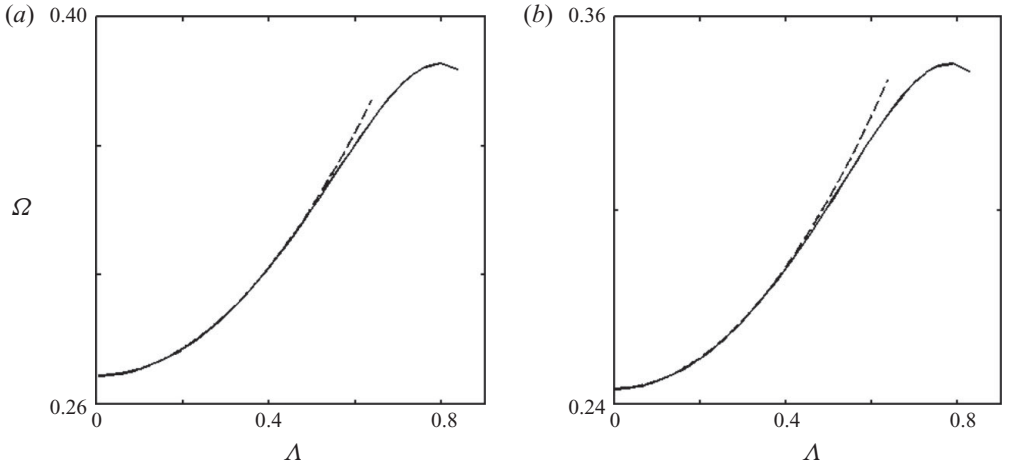

FIGURE 8. Comparison of frequency–amplitude correlation derived from perturbation analysis (– – – – –) and numerical iteration (——): (*a*) $N = 0$; (*b*) $N = \infty$.

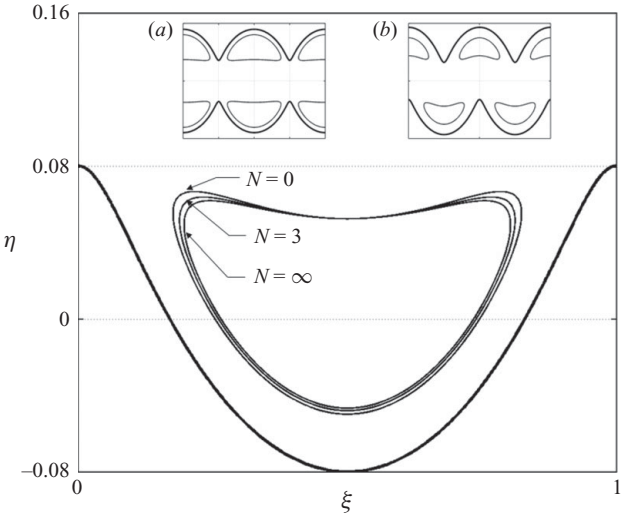

FIGURE 9. Effect of neighbouring vortices on vortex path in wavy-wall problem. The inset shows similar plots for (*a*) symmetrical wavy channel ($N = 0, 5, 10$) and (*b*) skew-symmetrical wavy channel ($N = 1, 5, 10$).

4.4. *Effect of neighbouring vortices*

We next examine the effect of having more than one vortex along the wall on the vortex path. The neighbouring vortices, separated by the corrugations of the wall, are in phase and thus move identically. Figure 9 shows, for the wavy-wall problem, the paths traced by a single vortex ($N = 0$) in comparison with the path traced by the same vortex with three neighbours on both sides ($N = 3$) and when there is an infinite number of vortices along the wall ($N = \infty$). The results suggest that the vortex motion is only weakly affected by the presence of neighbouring vortices, and thus increasing N has a diminishing effect on the individual vortex path. Essentially, the regular trajectories can be attributed to the lack of interactions between the isolated

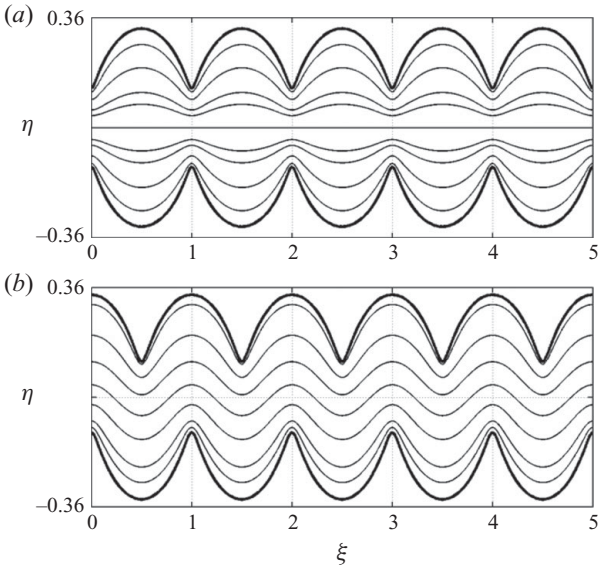

FIGURE 10. Particle trajectories under uniform flow field: (*a*) symmetrical wavy channel; (*b*) skew-symmetrical wavy channel.

vortices. Figures 9(*a*) and 9(*b*) present similar plots for the symmetrical wavy-wall channel and skew-symmetrical wavy channel respectively.

5. Lagrangian particle tracking

In this section, we examine the trajectories of particles released into the flow field at different distances from the wall. The wall amplitude and wavenumber for the wavy-wall problem is as previously set, whereas the channel parameters for both symmetrical and skew-symmetrical wavy channels are selected as $\epsilon = 0.35$ and $K = 0.45$, following Taylor (1981). For optimum mixing effect, vortex motion with maximum amplitude is desirable (Ottino 1989). However, vortices which move beyond the crest level can only be kept from being swept away by the uniform flow by means of external stirring. Hence, we limit the amplitude of motion such that the vortex chosen has a trajectory which remains within the corrugations.

5.1. *Lagrangian trajectories*

In the absence of vortex stirring ($\kappa = 0$), particles are purely advected by the uniform flow and thus trace the streamlines which follow the shape of the wall (figures 10*a* and 10*b*). In the symmetrical wavy channel (figure 10*a*), the particle located at the middle of the channel follows a horizontal trajectory, separating the channel into two non-interacting zones. The presence of vortices in the flow field alters the particle trajectories significantly, depending on particle initial positions. Figures 11(*a*)–11(*c*) show diverse particle motions under the stirring action of an infinite number of vortices for all three wavy configurations, where particles which are entrained by a vortex can be easily recognized from the looping in their trajectories.

For the wavy-wall problem (figure 11*a*), all four particles are observed to pass over the third trough without being entrained. One of the particles is entrained twice by the vortex in the second trough, and another trajectory is caught in resonance with the vortex in the fifth trough and is only ejected after a considerable time. Particle

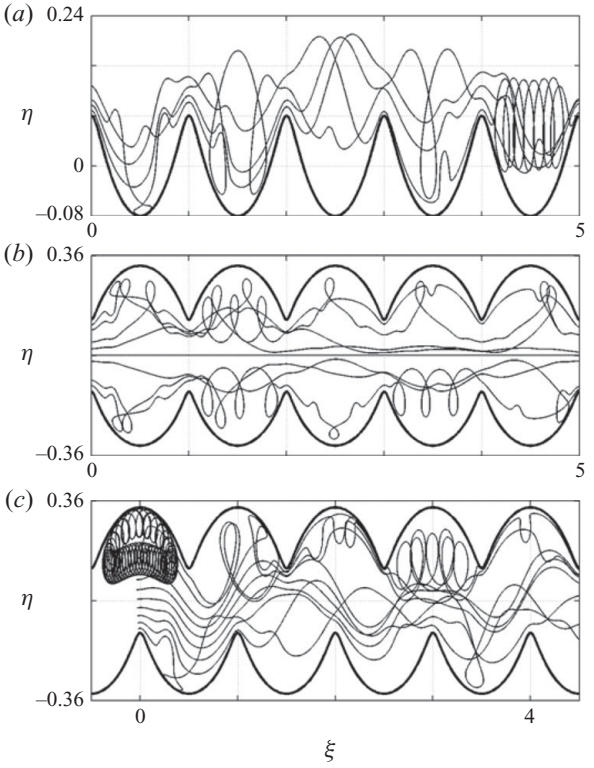

FIGURE 11. Particle trajectories for the case with infinite number of vortices in (*a*) wavy wall, (*b*) symmetrical wavy channel and (*c*) skew-symmetrical wavy channel.

distances from the wall are generally altered after each successive interaction with the vortices, regardless of whether particles are entrained or else oscillate slightly as they pass over each trough.

For the symmetrical wavy channel (figure 11*b*), the particle at the middle of the channel still traces a horizontal trajectory which forms an invariant centreline. Hence, the mixing efficiency of a symmetrical wavy channel is only comparable to that of a wavy wall bounded by a smooth wall on one side. In figure 11(*c*), nine particles are seeded into the skew-symmetrical wavy channel at $\xi = 0$, one of which is in close proximity to the vortex centre and is thus caught in extended resonance with the vortex motion. Here, an adaptive time step is adopted to resolve particle tracks in close proximity to the singular point at a vortex centre, and care is taken to avoid the singularity which is not of interest (or consequence) in the present study. We further note that (2.17) and (2.22) for particle motions in the symmetrical and skew-symmetrical wavy channels are only evaluated for finite values of N because a double infinite summation for vortices arising from the method of images combined with a second infinite summation for the array of vortices along the channel is not possible in analytic form. Hence, the case in which $N = \infty$ in the channel is replicated by employing periodic end boundary conditions with prescribed upstream ($x = 0$) and downstream ($x = \lambda$) limits. The value of N is arbitrarily chosen to be five to approximate, at reasonable computational cost, the vortex path where there are infinite number of vortices along the channel, recalling that further increasing N has a diminishing effect on the vortex trajectory (§4.4). The number of times

a particle exits and re-enters the computational domain is then tracked so that a continuous trajectory can be mapped to the physical domain. We stress that the periodic boundary condition serves to replicate a physical channel of infinite length with an infinite number of vortices in the flow direction and should not be taken as producing a closed system.

In figure 11, the observation of chaotic particle trajectories in all three wavy configurations indicates that the systems are indeed chaotic (Ottino 1989; Rom-Kedar *et al.* 1990). Since each vortex is trapped locally within a trough and does not interact with its neighbours except with its own image, the observed chaotic particle motion is attributed entirely to the unsteady motion of a single vortex in its locality. We note that if a finite number of vortices is employed along the wall or in the channel, then advected particles approach the vortex-populated furrows from the asymptotically simple region and eventually escape to the asymptotic region again. In either case, the systems exhibit transient chaos; i.e. chaotic scattering of advected particles occurs over a finite time on interaction with the vortices.

The Lagrangian chaos present in our model is in qualitative agreement with the laminar and transitional flow regimes for Reynolds numbers of 125 and 400 reported by Guzmán & Amon (1996) and Amon *et al.* (1996) for oscillatory flow in a sinusoidal channel. In both papers, the particle trajectories are determined by integrating the advection equation $\mathrm{d}\boldsymbol{x}/\mathrm{d}t = \boldsymbol{u}(\boldsymbol{x}, t)$, where $\boldsymbol{u}(\boldsymbol{x}, t)$ is the numerically simulated Eulerian velocity field, and exponential divergence of initially nearby particles is verified by positive finite-time Lagrangian Lyapunov exponents of selected test particles. Furthermore, the onset of Lagrangian chaos is associated with the first Hopf bifurcation. More recently, Biemond *et al.* (2008) showed, by means of a topological argument, that the onset of chaotic motion follows immediately the onset of periodic motion of the fluid, provided stagnation points are present in the flow. In § 6, we show that this is indeed the case for the present problem.

5.2. *Snapshots of particle positions*

Figures 12(*a*) and 12(*b*) provide snapshots of a line of 301 equally spaced particles advecting in the symmetrical wavy channel. Figure 12(*a*) shows the time evolution of the line of particles in the absence of any vortices. Unobstructed particles in the middle of the channel form a leading front which propagates downstream. As it traverses the converging and diverging sections of the channel, the flow undergoes alternate acceleration and deceleration and thus narrows and widens correspondingly. The width of the leading front eventually reduces, and particles nearer the walls increasingly lag behind, as they become held up in ever larger numbers of furrows. The line of particles is stretched in the diverging section of the channel and is folded at the wall corrugations. Particles along the upper and lower walls are of course symmetric about the invariant centreline.

In figure 12(*b*), the same line of particles is subjected to vortex stirring. In addition to stretching and folding, particles become dispersed. Particles near the walls soon break up from the leading front and become increasingly scattered. The non-entrained portion of the leading front is advected further ahead than in the previous case when there is no vortex in the flow field (see particle line for $t/T = 2$ and $t/T = 6$). This is due to the increased velocity induced by the counterclockwise rotating vortices at the upper wall and clockwise vortices at the lower wall. In contrast, entrained particles spend more time in the furrows. Consequently, these particles lag further behind the leading front than their counterparts in the case without vortices. Increased particle scatter is evident. Symmetry about the centreline is nonetheless maintained.

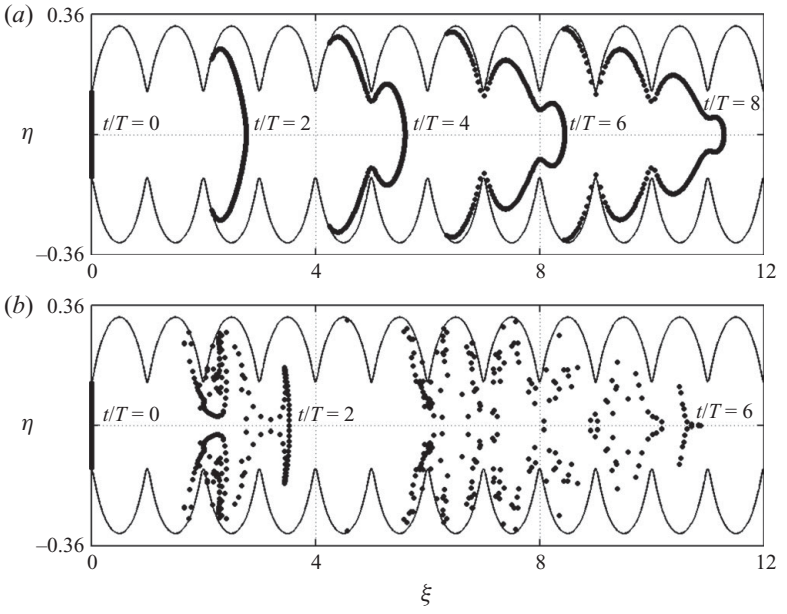

FIGURE 12. Snapshots of positions of a line of 301 particles (●) in the symmetrical wavy channel: (*a*) no vortices; (*b*) infinite number of vortices.

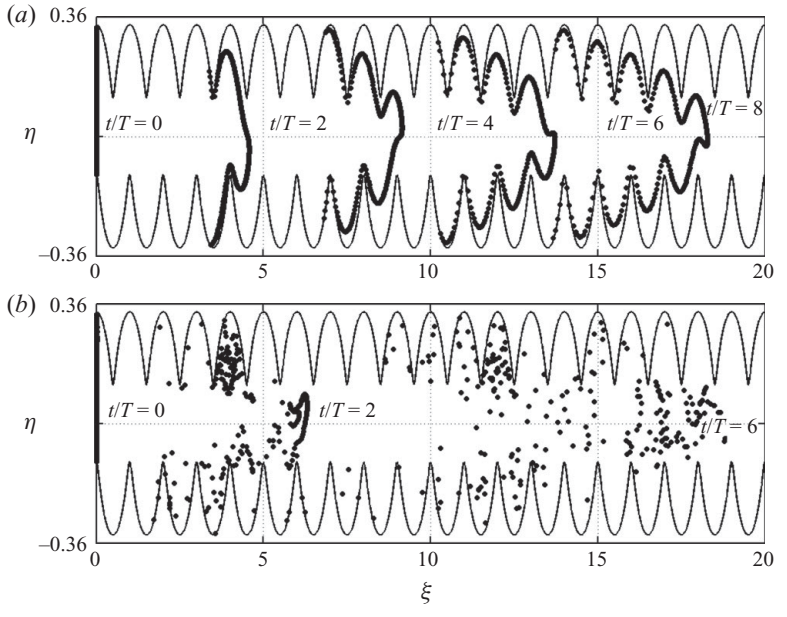

FIGURE 13. Snapshots of positions of a line of 301 particles (●) in the skew-symmetrical wavy channel: (*a*) no vortices; (*b*) infinite number of vortices.

Figures 13(*a*) and 13(*b*) show similar plots for the skew-symmetrical wavy channel. When there are no vortices (figure 13*a*), the line of particles deforms unevenly because of asymmetry, forming a leading front which is skewed in an oscillatory manner where the profile is influenced by the nearest corrugation. For the symmetrical wavy channel, the line of particles occupies an increasing number of furrows with time

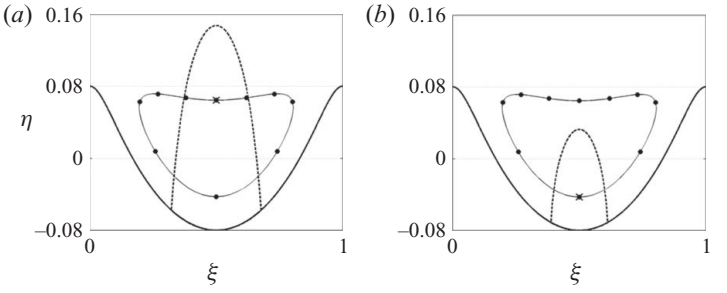

FIGURE 14. Vortex trajectory (——) and positions (●) at $T/10$ increment in a wavy trough. Also shown is the separation bubble (– – – – –) corresponding to the vortex position marked ×.

and is stretched and folded. Particles sufficiently distant from the wall are advected primarily under the influence of the uniform flow field and tend to traverse furthest.

In figure 13(*b*), vortical stirring is observed to obliterate the line of particles in less than two cycles (by $t/T = 2$). Similar to the symmetrical wavy channel, the leading front moves further ahead, whilst the entrained particles lag further behind. We note that certain particles initially located close to the vortex centre became trapped in the trough where they are released throughout the duration of the simulation. This agrees with the Lagrangian trajectories shown in figure 11(*c*) and those presented by Guzmán & Amon (1996) and Amon *et al.* (1996). Contrary to the symmetrical wavy channel, there is no symmetry in the particle distribution, and hence mixing can potentially take place across the channel width, making the skew-symmetrical channel superior to its symmetrical counterpart with regard to mixing efficiency. In § 7.2, we show that cross-centreline transport in the symmetrical wavy channel is possible if the effect of diffusion is included.

6. Dynamics of separation bubble

The mixing effect observed in § 5 can be associated with the presence of a separation bubble in the vicinity of the vortex, whose size and shape evolve continuously as the vortex moves. To examine the dynamics of the separation bubble, we consider a case involving a single furrow in the wavy wall, where $t/T = 0$ and $t/T = 0.5$ correspond to instants when the vortex is located at the highest and lowest positions respectively, in the middle of the furrow (figures 14*a* and 14*b*). The separation bubble is derived from the instantaneous streamlines separating an exterior region of positive stream function from an interior region of negative stream function. The separation bubble always joins the wall at two separation points, each of which constitutes an instantaneous stagnation point in the flow field. As pointed out in § 5.1, with the presence of stagnation points in the flow, the onset of chaotic motion follows immediately the onset of periodic motion of the fluid (Biemond *et al.* 2008).

6.1. *Variation of separation bubble size and vortex motion*

The size of the separation bubble A_b is derived from the physical domain and is normalized by its largest value at $t/T = 0$. Figure 15 shows that A_b reduces over half the cycle as the vortex moves clockwise and expands in the second half of the cycle. The time-dependent variation of A_b is closely related to that of the vortex vertical position y_v and the changes in distance between the two separation points (see inset in figure 15), both of which reduce from $t/T = 0$ to $t/T = 0.5$. The slight increase in A_b at the lowest point in the trough ($t/T = 0.5$) can be solely attributed

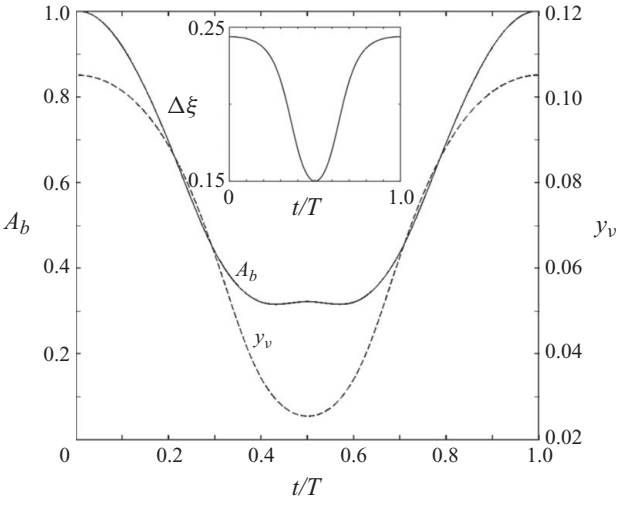

FIGURE 15. Temporal variation of the size of separation bubble A_b and vortex vertical distance y_v from the wall. The inset shows temporal variation of horizontal distance $\Delta\xi$ between the two separation points.

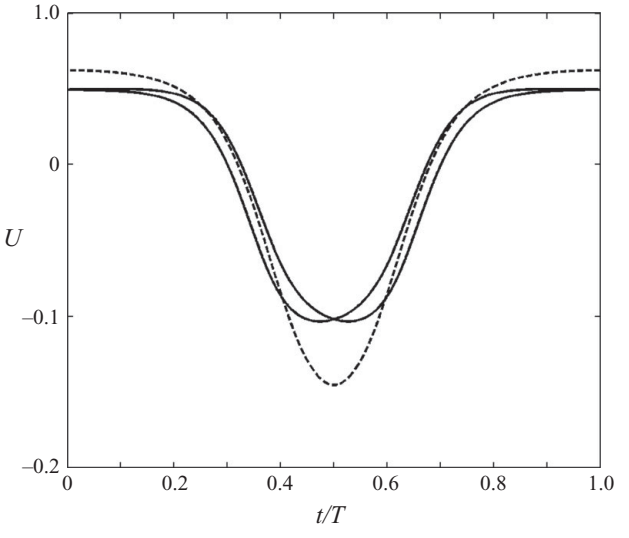

FIGURE 16. Temporal variation of longitudinal velocity U: – – – –, vortex; ——, separation points.

to the increase in wall curvature (figure 14). The changes reverse during the second half of the cycle, as expected. Overall, the size of the separation bubble varies by a factor of 3.1 over the cycle, implying that significant mass exchange is likely to take place across the separation boundary, favouring mixing as anticipated from the large-amplitude motion of the vortex.

Figure 16 shows the relative motion of the separation points with respect to the vortex. As the vortex traverses from $t/T = 0$ to $t/T = 0.3$, the separation points move slower than the vortex. From $t/T = 0.3$ onwards, the vortex starts to move upstream along the wall (see instantaneous vortex position in figure 14). The upstream

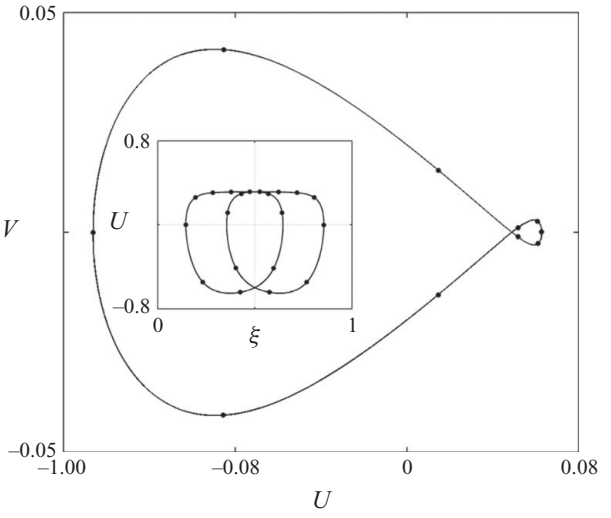

FIGURE 17. Velocity (U, V) of vortex tracked in the z-plane (● indicates $T/10$ increment). The inset shows velocity U of the two separation points with respect to their position ξ in the physical domain.

separation point moves ahead at a slightly larger velocity, whereas the downstream separation point trails behind (figure 16). On approaching the lowest point in the trough, the vortex velocity continues to increase at a higher rate compared with that of the two separation points. The inset of figure 17 shows the velocity U of the separation points with respect to their positions. When the vortex moves upstream close to the wall (lower half of the loop) U is twice that when the vortex moves downstream away from the wall (the plateau on the upper half of the loop). The factor of 2 is slightly less than that of the vortex motion where $U_{max}/|U_{min}| \approx 2.3$ (figure 16). Figure 17 also displays the velocity components (U, V) of the vortex. At $t/T = 0$, the vortex velocity in the x and y directions are $U = U_{max}$ and $V = 0$ respectively (rightmost point on plot). As the vortex rotates in the clockwise direction, V increases slightly and then changes to negative as the vortex moves downwards into the trough. Meanwhile, U reduces. By $t/T = 0.5$, U reaches its negative maximum, whereas V returns to zero (leftmost point on the plot). Whereas the magnitude of U varies by a factor of 2.3, that of V on the other hand varies by a much larger factor of 15.3. Relating the velocity of the vortex to its instantaneous position (figure 14), it is obvious that the sweeping motion along the wall (from $t/T = 0.3$ to $t/T = 0.7$) occurs rapidly compared with the downstream motion when the vortex is distant from the wall. This suggests that the vortex image has a dominant influence. In a complete cycle, the U–V plot thus resembles a highly distorted figure '8'.

6.2. *Particles escape from the separation bubble*

We proceed to examine the escape rate and particle trapping within the separation bubble. Particles are seeded into the separation bubble at equal intervals over the computational domain. The corresponding particle distribution in the physical domain is slightly distorted because of the mapping functions; however, this does not pose any issue for the present qualitative investigation. The number of particles used is in the order of 1000 for the case in which the initial vortex positions are set at $t/T = 0.5$. Retaining the same intervals, the number of particles used when the initial vortex

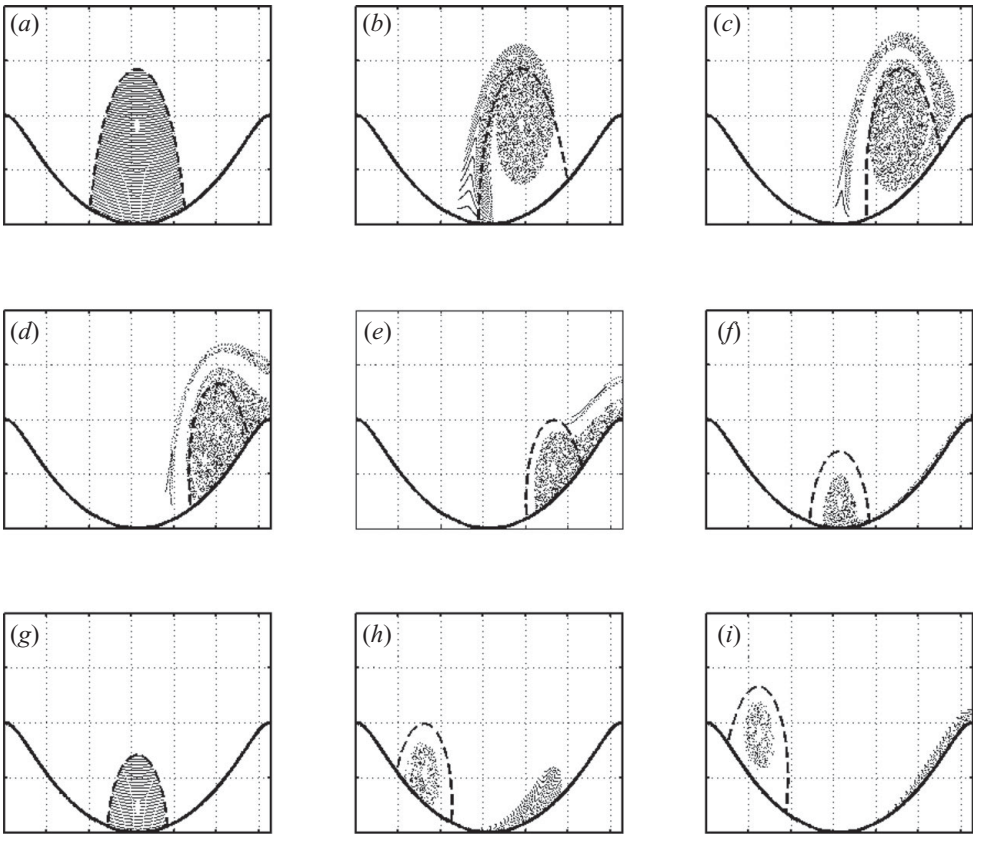

FIGURE 18. Sequential snapshots of particles escaping from within the separation bubble (– – – – –) in the wavy-wall problem (η versus ξ): (*a*)–(*f*) show the fate of particles seeded into the separation bubble from $t/T = 0$ through to $t/T = 0.5$ at $T/10$ increment; (*g*)–(*i*) show the fate of particles seeded into the separation bubble from $t/T = 0.5$ through to $t/T = 0.7$ at $T/10$ increment.

position is located at $t/T = 0$ is thus approximately a factor of 3 more, proportional to the increase in the bubble size. Adaptive time stepping is used to track accurately the particle trajectories in close proximity to the singular point in the vicinity of the vortex centre. Particles located within a distance of less than $0.05/\lambda$ from the vortex centre are discarded. These constitute less than 2 % of the total number of particles seeded.

Figure 18 shows sequential snapshots of particles escaping from within the separation bubble in the wavy trough, where the vortex initial position is set at $t/T = 0$. In figure 18(*b*), we can see that a large proportion of seeded particles is ejected from the downstream surface of the bubble in the first tenth of the cycle as the separation bubble moves to the right. These particles form a series of arrow-like features that point in the direction of their motion and tend to encircle the vortex. Particles to the left of the arrows have only moved minimally from their initial positions near the downstream surface of the bubble and lag behind as the vortex traverses. Particles to the right of the arrows, which originate from the now-white background in the separation bubble, have moved a considerable distance comparatively. We note that the arrow-like feature is an artefact of the finite number of particles followed. A compact blob would result if more particles are tracked

(see e.g. figures 26 and 28). The white background essentially represents particles outside the separation bubble, herein referred to as white particles. It can be observed that during this same time period, white particles sweep into the bubble rapidly from the upstream surface, curling past the vortex centre, suggesting that particles to the east of the vortex possess relatively larger velocity compared with those to the west, which is confirmed by the instantaneous velocity field (not shown). The boundary between white particles and seeded particles is the original separation boundary which is now greatly stretched under the stirring action of the vortex. Its deformed shape is akin to the unstable manifold numerically computed by Rom-Kedar *et al.* (1990) using the Melnikov technique for small perturbation. Further discussions on the stable and unstable manifolds in the present model are given in the next section. In figure 18(*c*) ($t/T = 0.2$), it can be seen that white particles have curled further, reaching the south-east of the vortex, effectively completing a loop around it. Note also that they have exited the separation bubble, and the leading front is attempting to re-enter the bubble. Meanwhile, the tail end of the train of particles still lingers in the vicinity of its earlier position. Figure 18(*c*) also shows the formation of a tongue-like feature which stretches downstream, leading eventually to particles escaping from the trough (figure 18*d*). When the vortex starts to sweep along the wall, it is relatively close to the downstream wall, which hinders particles from winding further around the vortex. Consequently, both seeded particles and white particles drain away under the action of the uniform flow (figure 18*e*). By $t/T = 0.5$ (figure 18*f*), the vortex centre is at its lowest position and is surrounded by the remaining seeded particles which are held in close proximity to the vortex centre thereafter. A considerable proportion of the separation bubble is now filled with white particles in the outer band. Re-seeding the separation bubble at $t/T = 0.5$ (figure 18*g*), figure 18(*h*) shows that within one tenth of a cycle, a large fraction of particles is swept downstream from the bubble as the vortex moves upstream at relatively high velocity. We note that the number of seeded particles which remains trapped around the vortex (figure 18*i*) is essentially the same regardless of whether re-seeding is performed at $t/T = 0.5$. This suggests that particles trapped are solely those initially in close proximity with the vortex centre, whereas re-seeded particles which fill the white band within the separation bubble in figure 18(*f*) are essentially all expelled. Hence, this confirms the presence of a non-escape zone which may be referred to as the vortex 'core', a generic feature of point-vortex dynamics (e.g. Babiano *et al.* 1994; Amon *et al.* 1996; Boffetta, Celani & Franzese 1996; Neufeld & Tél 1997, 1998). The series of snapshots in figure 18 also shows that white particles, though freely entering and escaping the separation bubble, cannot penetrate the vortex core occupied by seeded particles. This is due to the presence of irrational orbits known as Kolmogorov–Arnold–Moser tori, which act as transport barriers between the stable region in the vortex core and the unstable region outside (e.g. Rom-Kedar *et al.* 1990). Hence, the vortex singularity is essentially shielded by the surrounding regions of permanently trapped fluid and plays no role in the unsteady mixing process. Indeed the same dynamics would result if the vortex core is replaced by a non-singular vortex patch of constant vorticity whilst preserving the same total circulation. In § 7.2, we show that if diffusion is considered, it is then likely that particles within the vortex core will eventually escape (Chorin 1973). For the active-mixing problem (§ 8), the vortex core is exploited as a source of reacted catalytic particles with which approaching particles entering the separation bubble may react.

Figure 19 shows the fraction of particles trapped, n, as a function of non-dimensional time t/T in a fixed observation window which consists of a single trough.

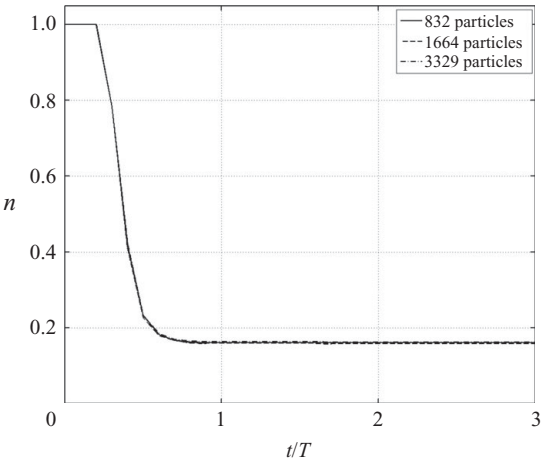

FIGURE 19. Fraction of particles trapped in the trough, n, as a function of non-dimensional time and effect of number of particles.

Particles seeded within the separation bubble escape primarily in the first cycle, after which there are only a few instances when a small number of particles are expelled as the vortex traverses past its lowest position at high velocities, causing those particles which fail to wind around the vortex to drift downstream. Figure 19 also shows that n is not sensitive to the total number of particles seeded. In a study of a continuously modulated free-surface flow, Wilson *et al.* (2006) reported equivalent temporal behaviour of the percentage of initial tracers remaining in seeded-eddy simulations in a study of mixing effects involving a separation bubble attached to a curved free surface. The drop in the tracer population is associated with the detrainment of fluid from the eddy region, whereas the flat plateau represents the entrainment phase, noting that the incoming fresh fluid is devoid of tracers. For large perturbation, as considered in the present study, a considerable proportion of the seeded tracers is ejected within the first cycle. The subsequent cascading reduction of tracer population obtained by Wilson *et al.* (2006) is however not obvious in our simulation, owing to the large perturbation adopted to optimize mixing. Rom-Kedar *et al.* (1990) obtained a similar finding from the simulated escape of particles from a lobe. Likewise, Wierschem & Aksel (2004) observed similar behaviour in an experimental study of the loss of fluorescent tracers from an eddy in a wavy corrugation.

Despite the foregoing discussion, we note that the calculation of n is based on the number of particles which remain in the trough instead of in the separation bubble. This explains why n only reduces after a short lag, because of the finite time taken for any of seeded particles to reach the downstream boundary of the observation window. Wilson *et al.* (2006) have used this approach to calculate n because the end of the domain is easier to define. We use the same approach in order to address boundary particles in the potential model. Should n be computed based on the fraction of particles that never leave the separation bubble, its value will not approach a constant but will alternate between two discrete values, the difference of which represents the small number of boundary particles which periodically enter and leave the separation bubble. Considering the case in which vortex motion commences from the position $t/T = 0$, boundary particles located to the east of the separation bubble are swept downstream, whereas those inside the separation bubble are ejected

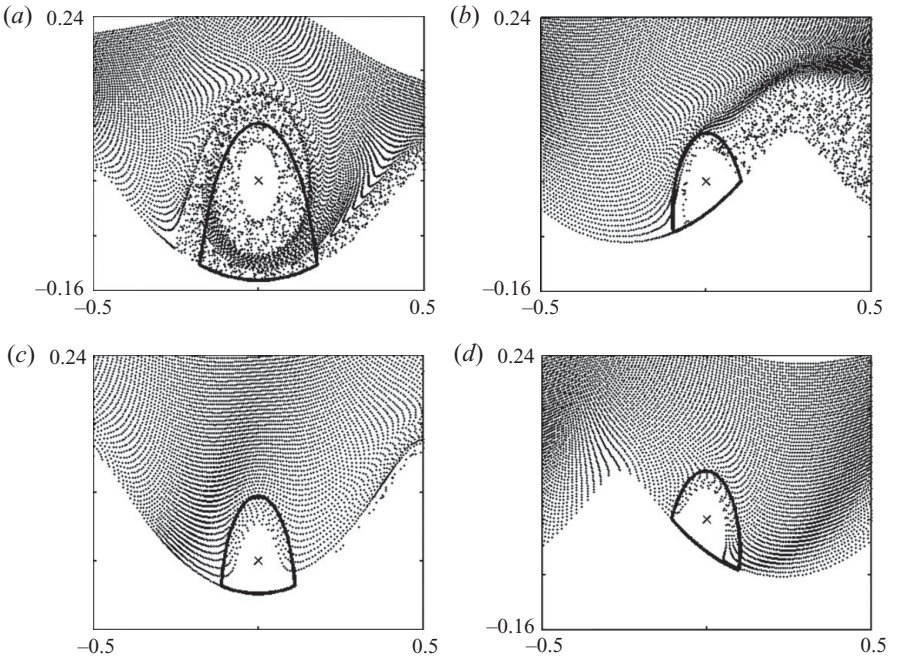

FIGURE 20. Instantaneous snapshots of particles' motion (●) on a reference frame co-moving with the vortex (×): (*a*) $t/T = 0$ or $t/T = 1$; (*b*)–(*d*) correspond to $t/T = 0.4$, 0.5 and 0.6 respectively. Note that the vacated zone in the vicinity of the vortex represents the vortex core (——, separation bubble).

upstream as the bubble moves in the opposite direction. This is because the wall is an invariant manifold, unstable downstream but stable upstream of the downstream separation point in the perturbed system of the vortex motion (Rom-Kedar *et al.* 1990). The opposing motion means that particles will inevitably become increasingly close to one another on the wall, forming a conglomerate point at plot resolution. For a wavy wall or channel that has an infinite number of vortices, a conglomerate point of boundary particles thus exists in each and every trough. These conglomerate points assume an oscillatory gliding motion along the wall upstream of the trough, entering and leaving the separation bubble periodically but unable to traverse the separation bubble.

6.3. *Mixing region, free-flow region and vortex core*

In the preceding section, it was observed that particles are able to enter and leave the separation bubble as it swells and shrinks. Substantial mass exchange between the flow and the separation bubble is induced by the stirring action of the vortex. Consider a large ensemble of particles seeded over four consecutive troughs horizontally extending up to elevation $y = 0.24$ in the z-plane. A single vortex is introduced in the rightmost seeded trough such that there is a continuous stream of particles approaching the vortex over one complete cycle. The region within $0.05/\lambda$ of the vortex centre, defined as the vortex core, is herein excluded. The motion of particles is observed using a reference frame moving with the single vortex, the initial position of which is set at $t/T = 0$.

As the vortex and particles are set in motion, particles entrained are greatly stretched and wind around the vortex at high velocities (figure 20*a*), resembling

the motion of white particles in figure 18(*b*). This results in a chaotic-sea-of-mixing region characterized by apparent particle scatter. The mixing region at this instant is significantly larger than the separation bubble and comparable to the size of the wavy trough. Mixed particles are subsequently ejected when the vortex sweeps downstream along the wall. We note that particles which have undergone mixing appear 'scattered' in the plots (figures 20*a* and 20*b*), whereas the others maintain a regular but distorted arrangement with neighbouring particles. Since no further particle entrainment occurs after $t/T = 0.4$, the size of the mixing region shrinks. By $t/T = 0.5$ (figure 20*c*), the mixing region is virtually non-existent, and it develops again shortly after $t/T = 0.6$ (figure 20*d*). Particles entering and leaving the separation bubble during these times do not wind around the vortex but stream past the vortex core. Indeed, the mixing region 'vanishes' from the plot as a result of the finite number of particles deployed. Our main interest in this context is the fact that the size of the mixing region varies greatly over half a cycle.

Whilst the snapshots of the ensemble of particles in figure 20 provide a glimpse of the mixing and free-flow regions (and indirectly the vacated, non-penetrable vortex core), the transient nature of chaos means that each of these regions is defined in terms of the respective sets of trajectories. We may thus construe the mixing region to be made up of a set of trajectories which wind around the vortex a finite number of times. Trajectories which never wind around the vortex constitute the free-flow region, and trajectories which infinitely wind around the vortex make up the vortex core (e.g. Rom-Kedar *et al.* 1990; Amon *et al.* 1996; Budyansky, Uleysky & Prants 2007). Trajectories of the mixing region and the free-flow region are responsible for mass exchange in and out of the separation bubble, whereas the vortex core behaviour is essentially isolated from the flow field. The free-flow region further out is not seeded and thus appears as a band of white particles in the upper part of the plots (see figure 20*a*). Particles in this region do not enter into the vicinity of the vortex or the trough and are advected mainly by the uniform flow with superimposed small oscillatory motion induced by the vortex. In the simulation shown above, all seeded particles pass the vortex after one and a half cycles. No particle is trapped, and none penetrate into the vacated vortex core.

Our present model of a unidirectional uniform flow field superposed with oscillatory vortex motion is analogous to aspects of oscillatory flow of a real fluid as studied by Sobey (1980) and Ralph (1986) using Navier–Stokes solvers. Sobey (1980) investigated the flow structure in wavy channels by considering different ratios of the oscillation amplitude to the mean flow amplitude. In the present study, the dimensionless amplitude for vortex motion is of the order of 0.6, 0.65 and 0.75 for the wavy wall, symmetrical channel and skew-symmetrical channel respectively under unit uniform flow. Hence, the cases considered herein approach the oscillatory unidirectional flows considered by Sobey (1980), where the ratio of the oscillatory component to the mean flow is taken to be of the order of $(1 - 0.55)/0.55 \approx 0.8$. Noting that the omnipresent vortex core is a non-interacting region, the birth of the mixing region is analogous to flow separation in oscillatory flow of a real fluid, which leads to vortex formation. During the first half-cycle, the separated region in the real fluid grows and the vortex bulges into the mainstream, eventually occupying most of the trough. The same behaviour is observed in the present model from $t/T = 0.5$ to $t/T = 1.0$. In the second half of the cycle, the real fluid flows into the upstream part of the furrow as the flow accelerates, thus displacing the vortex which is eventually eliminated as the bulk flow accelerates. Whereas the periodic shedding of vorticity is not relevant in our model, the process of vortex decay is replicated in the form

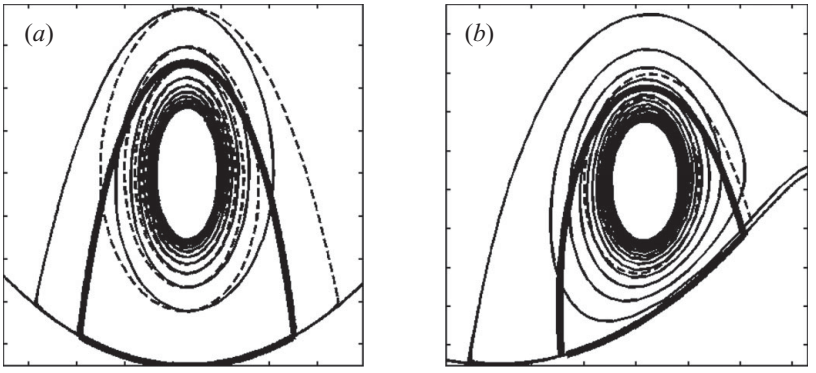

FIGURE 21. The stable (– – – –) and unstable (——) manifolds at (*a*) $t/T = 1.0$ and (*b*) $t/T = 0.3$. Here, the separation bubble is shown as the thick solid line.

of a vanishing mixing region that persists from $t/T = 0$ to $t/T = 0.5$. Essentially, the present model, which comprises a uniform flow with internally induced unsteady oscillation, produces the same dynamics in the periodic growth and elimination of the mixing zone as an externally induced unsteady oscillatory flow of a real fluid, noting that the qualitative flow behaviour is not sensitive to the wall profile (Sobey 1980). The similarity between the present results and the solutions of the unsteady Navier–Stokes equations by Sobey (1980) and Ralph (1986) lend much merit to the point-vortex model in the study of vortex-induced mixing.

6.4. *The invariant manifolds*

In this section, we endeavour to examine the unstable and stable manifolds in greater detail. Figure 21 shows exemplar plots of the instantaneous unstable and stable manifolds, numerically constructed by releasing a particle at each time step at the instantaneous hyperbolic points (i.e. the stagnation points A and B in figure 22) in the flow field in forward and backward times respectively. Particles starting on these invariant manifolds in the continuous time flow emerge as an infinite set of discrete points on these curves in the Poincaré section. In snapshots of a flow, the unstable manifolds appear as smooth curves. The stable manifolds, however, are not readily observable. Because of the symmetry of the system in space, these invariant curves are essentially mirror images of one another about the vertical axis through the middle of each furrow, for instance at $t/T = 1.0$ (figure 21*a*) and similarly at $t/T = 0.5$ (not shown). At other times, such as $t/T = 0.3$ (figure 21*b*), the mirror image of the curves about the vertical axis through the middle of the furrow gives the structure of the invariant curves at $t/T = 0.7$ owing to the symmetry of the system with time over a cycle, noting that the stable and unstable manifolds are thus swapped in the mirror image construction (figures 22*b* and 22*d*). Hence, the unstable manifolds for a flow from left to right become the stable ones for a flow from right to left, and *vice versa*.

In § 6.2, we have highlighted that the wall is an invariant manifold. With reference to figure 22, the unstable manifold to the east of point B and the two branches of the stable manifold towards point A (arrows in the figure indicate direction of particle motion along the invariant curves) lie exactly on the wall. In the unperturbed system, the unstable manifold of point A is also the stable manifold of point B, and its position coincides with the separation bubble, thus separating the exterior free-flow region and the interior region. In this case, the manifold structure is topologically equivalent to one half of the oscillating vortex-pair flow (e.g. Rom-Kedar *et al.* 1990;

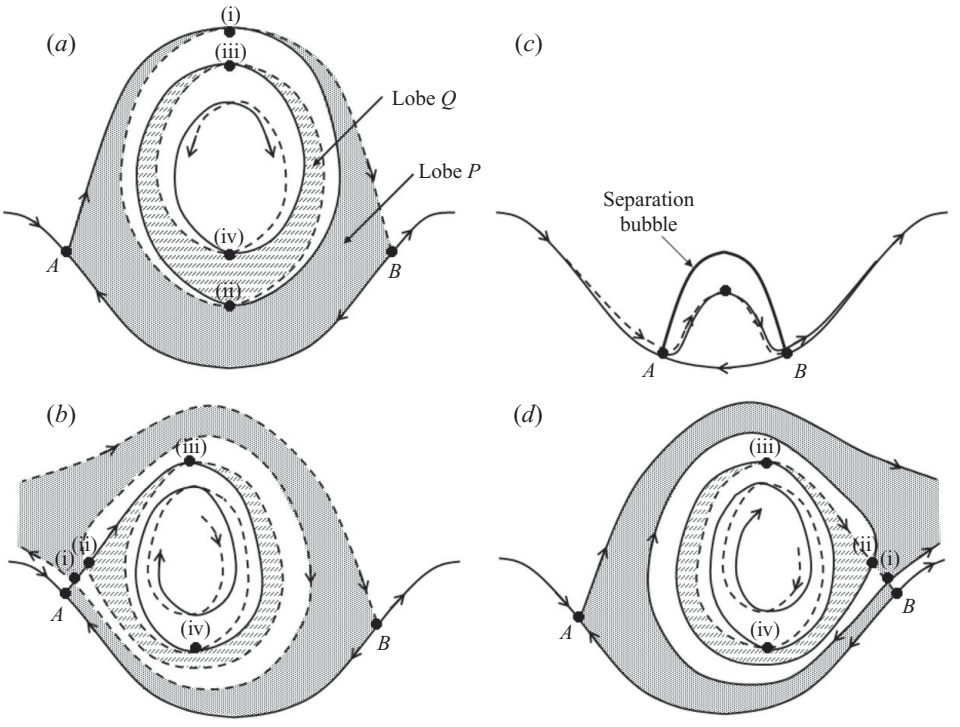

FIGURE 22. Schematic illustration of the stable (– – – – –) and unstable (——) manifolds at (*a*) $t/T = 1.0$, (*b*) $t/T = 0.3$, (*c*) $t/T = 0.5$ and (*d*) $t/T = 0.7$. The two shaded areas bounded by segments of the unstable and stable manifolds defined by the intersection points (i), (ii), (iii) and (iv) represent two different lobes which transport the fluid contained as the invariant curves traverse with the vortex motion. For clarity, only the separation bubble of (*c*) is shown.

Rom-Kedar & Wiggins 1990; Wilson *et al.* 2006). When the system is perturbed, the spiral nature of the invariant manifolds produces infinite self-similar criss-crossing tangles at all scales (figures 21 and 22). In the discussions that follow, we wish to highlight the role of the infinite set of intersections between the stable and the unstable manifold in the mechanism for mass transfer into and out of the mixing region. In § 8, we investigate the fractality of the invariant manifolds.

Since no flow is able to cross the invariant curves except by diffusion only (which will be considered separately in § 7.2), the invariant curves divide the flow field into a free-flow region in the exterior and a recirculating zone in the interior (which comprises the mixing region and the vortex core). A parcel of fluid bounded by a segment of the unstable manifold and a segment of the stable manifold between two successive intersection points can be defined as a 'lobe' where the fluid which lies within it remains there for all time (e.g. Rom-Kedar *et al.* 1990; Rom-Kedar & Wiggins 1990; Wilson *et al.* 2006). Figure 22 shows the evolution of two lobes as the invariant curves traverse with the vortex. Note that figures 22(*a*) and 22(*c*) match the time instants of figures 20(*a*) and 20(*c*) respectively. On the other hand, figures 22(*b*) and 22(*d*) are at different times from those in figures 20(*b*) and 20(*d*) in order to facilitate visualization of the invariant curves. Figure 22(*b*) shows that lobe *P* carries the fluid parcel from the upstream into the recirculating zone. Driven by the growing unstable manifold, the fluid in lobe *P* subsequently undergoes mass exchange in and out of the separation bubble but remains contained within the outermost invariant

manifolds; that is, the invariant manifolds cover a region significantly larger than the separation bubble during these times (see figures 20*a* and 22*a*). When the lobe reaches the downstream end of the trough, the stable manifold starts to contract. Consequently, the lobe is ejected together with the bounding segments of the unstable manifold (figure 22*f*). Lobe Q undergoes the same processes as lobe P except that it grows earlier, shrinks later and contains a smaller quantity of fluid. Hence, particles closer to the vortex centre are entrained longer. Note also that the lobes enter and leave the separation bubble a finite number of times from their ingestion to their eventual ejection.

Just before the vortex reaches its lowest position (at approximately $t/T = 0.4$), the stable manifold contracts to a minimum, and the last remaining lobe is stretched in the direction of the unstable manifold, draining the fluid it contains downstream. When the vortex starts to move upwards from its lowest position, a new lobe is entrained along the stable manifold of the hyperbolic point B. At this instant ($t/T = 0.5$), there is only a single intersection between the new stable manifold and the diminishing old unstable manifolds (figure 22*c*). A new unstable manifold grows immediately after the old one detaches from the hyperbolic point A (at approximately $t/T = 0.6$). During the transition, the region covered by the invariant curves is smaller than the separation bubble, which relates well to figure 20(*c*).

Wilson *et al.* (2006) have shown that the entraining lobe and the detraining lobe can be overlapped. They have observed that under large perturbation, self-intersecting turnstiles are responsible for ejection of fluid ingested during the same cycle. The mechanism is similar to that shown in figure 18. A close examination of the evolution of the lobes in figure 22 suggests that the same lobe undergoes the entraining phase from $t/T = 0.5$ to $t/T = 1.0$ (or equivalently from $t/T = -0.5$ to $t/T = 0$) and the detraining phase from $t/T = 0$ to $t/T = 0.5$. In fact, owing to the spiral structure of the invariant curves, the exterior and the interior of the lobes cannot be distinguished. For the same reason, the 'turnstile' structure in the vicinity of the hyperbolic points is also different from that described by Rom-Kedar & Wiggins (1990) and Wilson *et al.* (2006). Here, the same lobe (e.g. lobe P) undergoes simultaneous contraction from both sides of the unstable manifold during the entraining phase (figure 22*b*) and later simultaneous stretching at both sides of the stable manifold during the detraining phase (figure 22*d*). Experimentally, Wierschem & Aksel (2004) have shown that the turnstile lobe mechanism is responsible for the breakup of the separatrix, thus permitting a spiralling inflow and outflow motion which governs the material exchange between the eddy in the furrow and the overlying steady flow.

7. Mixing efficiencies

7.1. *Statistical dispersion of passive particles*

This section compares the mixing efficiencies of the three different configurations: the wavy wall, symmetrical wavy channel and skew-symmetrical wavy channel. In each case, about 7000 particles, equally spaced in the z-plane, are seeded within one wavelength with a mean initial position of $\overline{x} = \lambda/2$ ($\overline{x} = 0$ for the case of skew-symmetrical channel), vacating the region within $0.05/\lambda$ from the vortex centre. We employ an infinite number of vortices with maximum amplitude of motion contained within the trough. Particles seeded are tracked for 10 cycles, and the standard deviation σ of their positions along the axis of the channel is calculated as a function of time. From figure 23(*a*), it can be seen that σ increases monotonically with time for all three cases (e.g. Sobey 1985). In the wavy-wall problem (particles

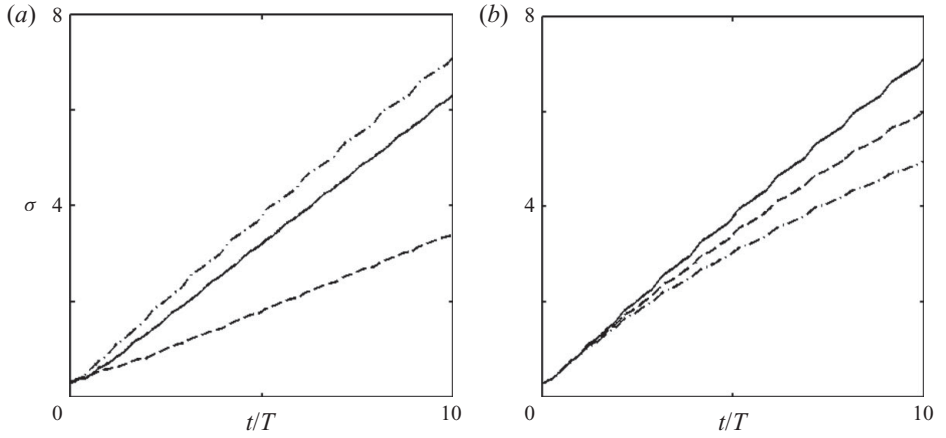

FIGURE 23. Mixing efficiencies measured in terms of standard deviation σ. (*a*) Comparing wavy wall (——), symmetrical wavy channel (– – – – –) and skew-symmetrical wavy channel (–·–·–·–). (*b*) Effect of diffusion on passive mixing in skew-symmetrical wavy channel: $\nu = 0$ (——), $\nu = 0.001$ (– – – – –), $\nu = 0.005$ (–·–·–·–) .

seeded up to $y = 0.24$), we note that particles steadily drift further away from the wall and thus have diminishing interactions with the vortices trapped in the wall corrugations. Therefore, the wavy-wall configuration is not desirable for long-term or long-range mixing. The skew-symmetrical wavy channel outperforms the symmetrical wavy channel with significantly higher values of σ. In addition, the latter does not allow lateral mixing across the invariant centreline shown in figure 24(*a*), whereas the former permits cross-centreline mixing as illustrated in figure 25(*a*). In conclusion, the skew-symmetrical wavy channel is the most efficient in passive mixing (e.g. Nishimura & Matsune 1996).

7.2. *Diffusion by random walk*

The particle tracking scheme presented above models only the advection of passive tracers. Chorin (1973) proposed that advective and diffusive phenomena could be treated separately, where the latter may be simulated using a stochastic technique involving random particle displacements analogous to Brownian motion. It is assumed that at the end of every advective step, each particle undergoes a random walk in two orthogonal directions. The standard deviation of these random walks must be compatible with the analytical Gaussian solution of pure diffusion, and therefore the fluctuating random velocity components of a particle are written as

$$u_r = r_1\sqrt{2\nu/\Delta t}, \quad v_r = r_2\sqrt{2\nu/\Delta t}, \tag{7.1a, b}$$

where the subscript r indicates random component; ν and Δt are the diffusion coefficient and time step respectively; and r_1 and r_2 are independent normally distributed random numbers, each with zero mean and unit standard deviation (e.g. Borthwick & Barber 1992).

Owing to the fact that the distribution of the random number generated will inherently be distorted by the mapping functions, the random walks are performed based on length of displacements in the physical domain instead of the computational domain. Equations (7.1) are thus rewritten as

$$\Delta\xi_r = u_r\Delta t, \quad \Delta\eta_r = v_r\Delta t, \tag{7.3}$$

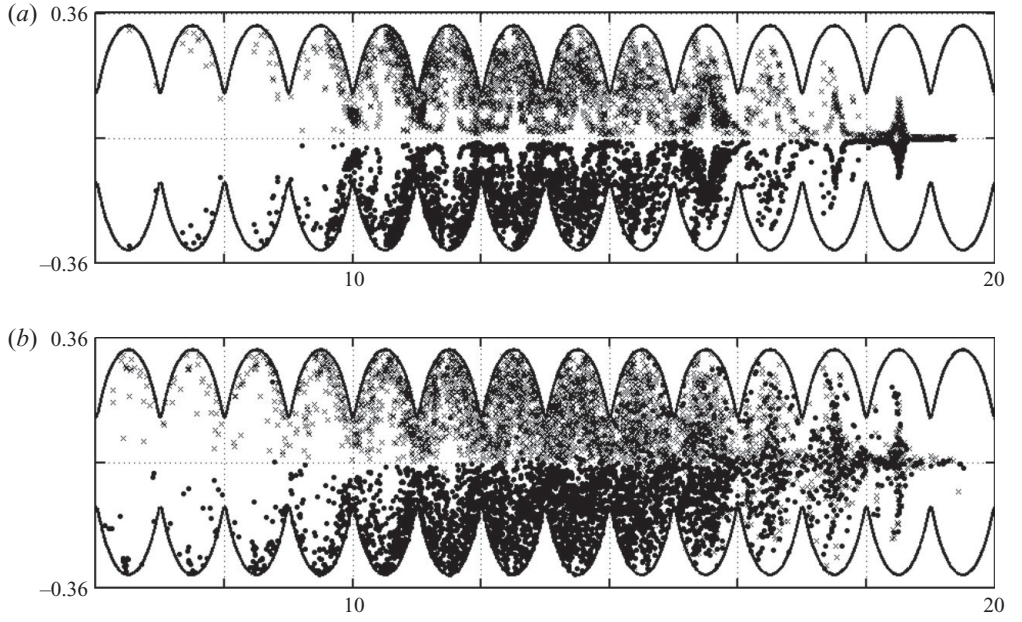

FIGURE 24. Particle positions at $t/T = 10$ for symmetrical wavy channel (η versus ξ): (*a*) $\nu = 0$; (*b*) $\nu = 0.001$. (Initial particle positions are equally spaced in the z-plane within one wavelength with mean position $\overline{x} = \lambda/2$; $\times$ and ● represent initial particle position above and below the centreline respectively.)

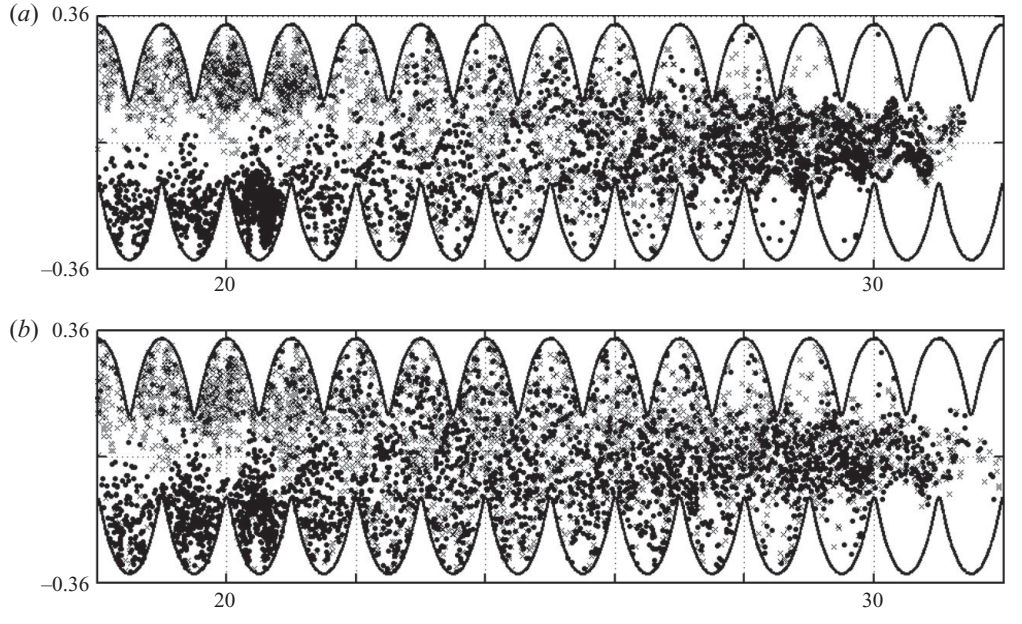

FIGURE 25. Particle positions at $t/T = 10$ for skew-symmetrical wavy channel (η versus ξ): (*a*) $\nu = 0$; (*b*) $\nu = 0.001$. (Initial particle positions are equally spaced in the z-plane within one wavelength with mean position $\overline{x} = 0$; $\times$ and ● represent initial particle position above and below the centreline respectively).

where u_r and v_r are the random velocity components in the ζ-plane. It follows that the crux of the method lies in the inverse mapping of the particle position at the end of each random walk in order to proceed with the Lagrangian tracking. As there are no closed-form solutions of the inverse mapping functions for all three cases, namely the wavy wall and the symmetrical and skew-symmetrical wavy channels, the corresponding particle position in the z-plane is iteratively solved on the basis of the orientation and magnitude of displacement which are kept conformal by the mapping functions. In order to maintain the validity of the statistical distribution, all particles are solved using the same time step, which is chosen to be small ($\Delta t = 0.001$) in order to minimize the non-physical tendency of particles in the numerical solutions to cross the flow boundary or penetrate the vortex core. The few particles which do start to cross the boundary are halted at the boundary itself, whereas particles which enter the vacated vortex core are returned to their initial positions and subjected to a fresh attempt.

Figures 24(b) and 25(b) show the particle positions at the end of the 10th cycle for the symmetrical and skew-symmetrical wavy channels for $\nu = 0.001$. Increasing scatter with the magnitude of diffusion coefficient is evident when $\nu = 0.005$ is used (not shown). For the symmetrical wavy-wall problem, cross-centreline mixing is now possible, resulting in qualitative mixing which resembles the effect produced by the skew-symmetrical wavy channel with zero diffusivity (figure 25a). Introduction of diffusion by random walks causes the skew-symmetrical wavy channel to produce even better particle scatter, notably in the lateral direction. Figure 23(b) shows the standard deviation as a function of time when different diffusion coefficients are used for the skew-symmetrical wavy channel. The same is observed for the symmetrical wavy channel. The decrease of σ with increasing diffusion is counter-intuitive but well founded. In figures 12(b) and 13(b), we have shown that under the influence of an infinite number of vortical stirrers, a line of particles spreads further longitudinally, with particles at the rear predominantly engaged in hydrodynamic resonance and particles at the front mainly undisturbed. Because of diffusion, particles at the rear are now more likely to escape from the vortex core and mixing zone to the free-flow region, rejoining the bulk flow. On the other hand, particles at the front that are sufficiently distant from the vortex field at most instants may now be entrained owing to diffusivity or even penetrate the vortex core and become permanently trapped. These particles then lag behind, reducing the number of particles in the leading front. The combined effect thus gives an overall reduction of σ which quantifies longitudinal particle dispersion.

8. Active mixing

The preceding investigation focuses on passive tracers which are able to follow the physical flow behaviour and be transported with negligible influence on the flow regime regardless of the concentration. The tracers are inert and demonstrate no growth or decay in their course of motion. In practical conditions, however, passive tracers of distinct characteristics may exhibit chemical or biological interactions with the fluid and/or other constituents. In particular, autocatalytic reactions are those in which at least one of the products is a reactant and of which the rate equations are fundamentally nonlinear.

The simple autocatalytic reaction $A + B \longrightarrow 2B$ in a chaotic flow regime was first investigated by Metcalfe & Ottino (1994) for flow in a bounded eccentric cylinder. Their work captured the growth and propagation of patterns in active mixing driven

primarily by the highly interwoven nature of the manifold tangle. Toroczkai *et al.* (1998) and Károlyi *et al.* (1999) extended the study to open chaotic flow around a cylinder and showed that the fractal unstable manifold in the wake of the cylinder acts as a catalyst for the process. A fractal object is highly ramified such that its surface area (or perimeter in the case of two-dimensional object) is resolution dependent. As a result, reactions occur only at the fractal boundary and mixing is imperfect. Budyansky, Uleysky & Prants (2004) studied a simple two-dimensional open flow composed of a fixed point vortex and a background periodic current and showed that the tracer dynamics is typically chaotic in the mixing region. The boundary of the vortex core acts as a dynamical trap for advected particles, resulting in a fractal-like scattering function which depends on the trapping time. Indeed, the mixing problem considered herein is an open-flow problem characterized by transient chaos and permanent fractality (Károlyi & Tél 2007).

We now extend our study to active mixing where the non-escaping vortex core acts as the source of the reacting seed. The effect of the vortex dynamics on the overall mixing mechanism and efficiency will be investigated using the surface reaction theory of Károlyi *et al.* (1999).

8.1. *Numerical implementation of autocatalytic reaction*

We consider the autocatalytic reaction $A+B \longrightarrow 2B$ in a wavy channel with an infinite number of vortices, where a single-vortex core is selected to carry a finite number of seed particles B which are incapable of escaping. The incoming background flow constitutes A particles, which will react and be transformed to B particles if they come within a prescribed reaction distance ϵ_0 from the existing B particles in the flow field. These B particles are produced in the mixing zone and are thus capable of being ejected from the vortex and advected downstream, reacting with other A particles they come in contact with.

One way to numerically simulate the above processes is to adopt a uniformly gridded domain with each cell being occupied by either type A or type B particles, regardless of the actual number of particles present. If both species are present, then B always survives. At a prescribed reaction rate, the neighbouring cells of a cell occupied with B particles will be converted if they are not already B-type cell (e.g. Toroczkai *et al.* 1998; Péntek *et al.* 1999; Liang, Taylor & Borthwick 2007). After the reaction stage, particles occupy the positions of their respective cell centres and resume passive advection until the next reaction sets in. The grid size must thus be less than or equal to the reaction distance ϵ_0. In the present model, the uniform grid is constructed in the physical ζ-domain, and hence the corresponding grid points in the computational z-domain must first be established via inverse mapping. Both passive and active processes are computed entirely in the z-plane, and mapping to the ζ-plane is performed for graphical purposes only.

An initial patch of 400 B-type particles is seeded inside the vortex core. A grid size of $\epsilon_0 = 0.05/\lambda$ is adopted, equivalent to 0.36 % of the wall wavelength. The observation window covers five wavelengths, with the reacting vortex core in the first. The vortex motion always commences from its lower middle position (corresponding to the position at $t/T = 0.5$, in § 6) for all reaction rates. For reaction rates shorter than the periodicity T of the vortex motion, an integer number of reactions per cycle is considered; for reaction rates longer than T, the reaction rate is taken to be an integer multiple of T. This ensures that behaviour which repeats at the period of the vortex motion appears as fixed points, or periodic cycles, on the stroboscopic map taken at the instant of the reaction (Károlyi *et al.* 1999).

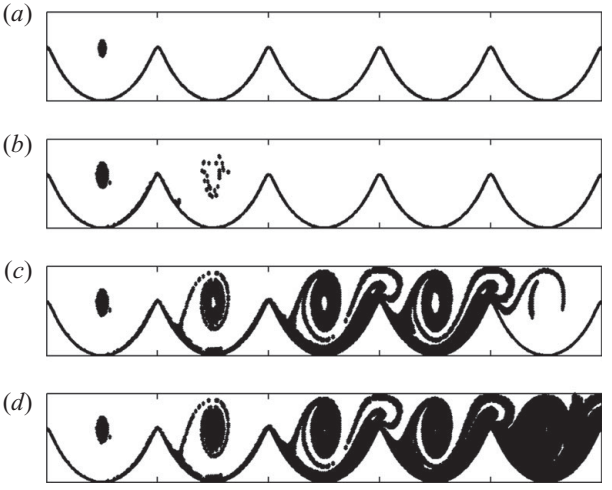

FIGURE 26. Evolved seed patch of reacting B particles in the symmetrical wavy channel at two reactions per cycle (η versus ξ; plots show lower half of the channel only): (a)–(d) correspond to $t/T = 0.5, 2.5, 4.5$ and 8.5 respectively, where initial vortex position ($t/T = 0$) is at its nearest to the wall.

8.2. *Fractal dimensions and reaction theory*

Figure 26 shows evolved B particles seeded in the symmetrical wavy channel considered at two reactions per cycle. Figure 26(a) shows that within the first half a cycle, species B grows in the vortex core but no particles have yet escaped the vortex field as it grows (refer §6.3). At the end of the first cycle, as the vortex sweeps down the trough at large velocity, a substantial amount of B particles drain along the wall. These particles are advected into the second trough and subsequently entrained by the vortex in the neighbouring trough (figure 26b). The second vortex is eventually infected and acts as another source of the seed particles (figure 26c). As the process continues, accelerated reaction with background A particles produces an increasing number of B particles which escape along the unstable manifold. A quasi-equilibrium state is eventually reached after four cycles where the number of B particles produced, n_B, is balanced by the number that have escaped from the observation window (figure 27, inset). However, the vortex in the fifth trough does not operate as a reaction site, being surrounded by B particles. The above reaction rate is relatively low, and we note that B particles do not cross the centreline of the channel.

The structure observed in figure 26 clearly resembles the unstable manifold shown in figure 21. Amongst others, Károlyi *et al.* (1999) have found that active particles trace out the unstable manifold but with wider coverage due to the advancing reaction process. This means that the reactions occur on the surface of the fattened-up unstable manifold of the chaotic saddle, which has a fractal appearance with filamental structures. Although the chaos is transient in the mixing region, the fractal pattern traced out by the reactions is permanent and can be quantified with a fractal dimension D_0 (Péntek *et al.* 1999). Furthermore, this fractal dimension is the same as that of the unstable manifold in the reaction-free flow.

The continuous reaction equation for an autocatalytic reaction in an open flow proposed by Károlyi *et al.* (1999) is

$$\dot{A}_B = -kA_B + g_e(t)(2 - D_0)v_r A_B^{-\beta}, \tag{8.1}$$

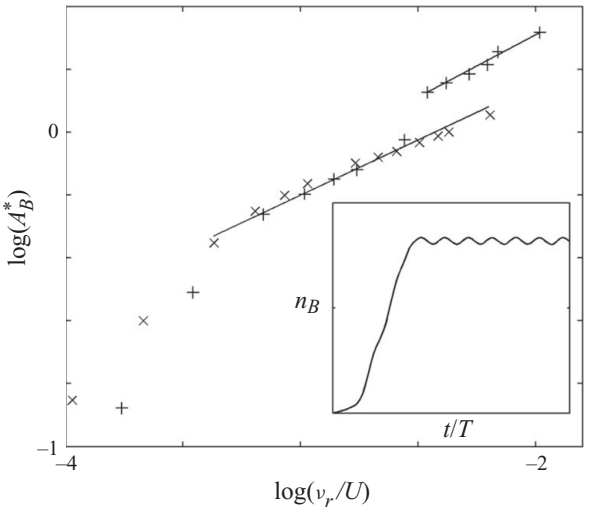

FIGURE 27. Power scaling law of the steady-state reactant front area: +, symmetrical channel; ×, skew-symmetrical channel. The inset shows typical temporal growth of the population of B particles inside the observation window.

where A_B is the area covered by reacting B-particles within the observation window; k is the escape rate of the particles; $g_e(t)$ is a geometrical factor containing information on the unstable manifold; v_r is the reaction front velocity ($= 2\epsilon_0/t$); and t is the lag time between reactions. The positive exponent β is defined as $(D_0 - 1)/(2 - D_0)$, with $1 < D_0 < 2$. The first and second terms on the right-hand side of (8.1) describe the escape and the production respectively of B particles. If the reaction takes place on a simple non-fractal line, i.e. $D_0 = 1$, then $\beta = 0$ and (8.1) reduces to classical surface reaction (Landau & Lifshitz 1987). In chaotic open flow, the boundary of the unstable manifold is fractal, where $D_0 > 1$. Consequently, the reaction described by (8.1) is dissipative and possesses an attractor. Solving for the steady solution ($\dot{A}_B = 0$), we have a trivial unstable equilibrium if $A_B^* = 0$ or

$$A_B^* = [g_e v_r (2 - D_0)/k]^{(2-D_0)}. \tag{8.2}$$

Equation (8.2) describes the steady-state condition achieved when newborn and escaping particles are balanced. The fractal dimension D_0 can be easily determined because the slope of the log–log plot of A_B^* versus v_r is $(2 - D_0)$ (figure 27).

We consider reaction rates ranging from 1/2 to 30 reactions per cycle for both the symmetrical and skew-symmetrical wavy channels (figure 27). The area occupied by B particles is simply given by $n_B \epsilon_0^2$. Plotting the same data in figure 27 using normal scale (not shown), extrapolation gives zero B particles as the reaction front velocity reduces to zero. There is a linear increase of B particles up to two reactions per cycle, beyond which the production rate decreases because of competition from the particle escape rate from the observation window. For a reaction rate $\leqslant 1$ per cycle, the reactions take place at a fixed site, corresponding to the initial position of the vortex at the middle lowest of the vortex trajectory. Should the reaction site be changed, different results would be obtained. This corresponds to the zone $v_r/U < 3.5 \times 10^{-4}$ in figure 27. Sensitivity checks confirm that the selection of reaction site has negligible effect on the resulting area occupied for reaction rates $\geqslant 2$ per cycle, which constitutes our region of interest. The fractal dimension D_0 in this region is approximately 1.65,

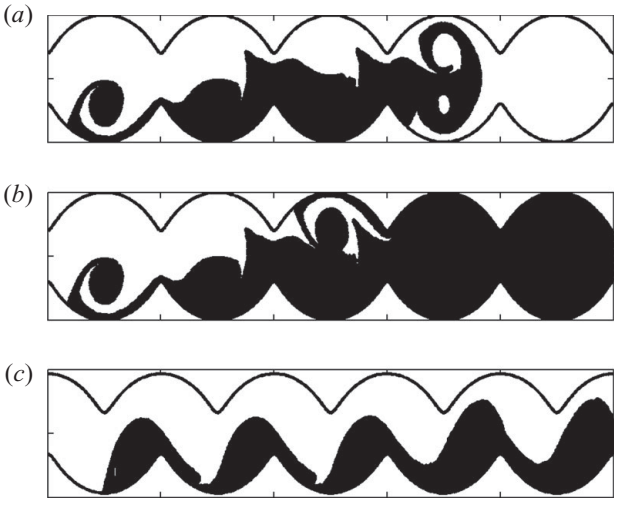

FIGURE 28. Evolved seed patch of reacting B particles at 20 reactions per cycle (η versus ξ) for the following: symmetrical wavy channel at (a) $t/T = 2.5$ and (b) $t/T = 4.5$; (c) skew-symmetrical wavy channel at $t/T = 3.75$. The initial vortex positions ($t/T = 0$) are at their nearest to the wall.

which implies that the reaction rate is slow on the characteristic scale of chaotic advection and verifies the singular enhancement of productivity (Toroczkai *et al.* 1998; Károlyi *et al.* 1999). It is interesting to note that for reaction rate $\geqslant$10 per cycle, the symmetrical channel shows a sudden increase of A_B^* and thus an offset in figure 27. This region of higher reaction rates has a fractal dimension of 1.60 which is slightly different from the intermediate reaction rate. The augmentation of the area covered can be attributed to the entrainment of B particles by the vortex at the opposite wall immediately after the particles cross the converging part of the channel and are confronted by the swelling separation bubble (figure 28a). The opposite vortex core gradually becomes infected, and as a consequence, more troughs are completely filled with B particles when the quasi-equilibrium state is attained (figure 28b). In the skew-symmetrical channel, despite the fact that B particles regularly visit the opposite side of the channel, they are not entrained. Figure 28(c) shows that B particles intrude into the upstream end of the upper trough when the vortices at the lower wall are at their rightmost positions. At this instant, the upper vortex fields are also located at the rightmost positions near the downstream end of the troughs. As a result, particles do not encroach into the upper vortex field. At the next instant, protruding B particles are drawn back by the lower vortices when the vortices at both upper and lower walls sweep down the wall (counterclockwise and clockwise respectively), and the separation bubble contracts. Similarly, when the lower vortices are at their leftmost positions, B particles intrude the downstream end of the upper trough (not shown). At the same instant, the upper vortices are also located at their leftmost positions; i.e. the vortex fields are near the upstream end of the troughs, unable to entrain B particles at the opposite end. Hence, in the absence of the dynamics induced by the converging-diverging flow field, the serpentine-type skew-symmetrical channel maintains a boundary between A and B particles on the upper and lower walls respectively for reaction rates up to 30 per cycle.

It is interesting to note that the fractal dimension obtained above shows grid independence when a coarser cell of size $0.1/\lambda$ is used. Moreover, the simulations are

at the limit of weak diffusion, where the reaction range is of the same order as the diffusion distance for $\nu = 0.005$ (§ 7.2). We note that for two-dimensional hyperbolic open systems, the fractal dimension can be related to the escape rate k and the Lyapunov exponent λ_n via (Tél *et al.* 2005)

$$D_0 = 2 - k/\lambda_n. \tag{8.3}$$

For a quantitative characterization of the escape rates, the ensemble of particles in figures 24 and 25 is monitored to determine the fraction n retained within the trough of their origin as a function of time. In both cases, exponential decay is observed and can be fitted with the correlation $n \sim \exp(-kt)$, giving $k \sim 0.031$ and 0.030 for the symmetrical and skew-symmetrical channels respectively. Exponential decay of material from an eddy in a wavy corrugation has been verified experimentally for a range of flow parameters by Wierschem & Aksel (2004). The Lyapunov exponent, which gives the rate of stretching of nearby particles, is measured by starting a test particle close to that of a reference trajectory with an initial distance of $\delta = 10^{-5}/\lambda$. Whenever the distance of the test particle from the reference trajectory is larger than a threshold value of 10δ, it is shifted back to a distance δ from the reference trajectory along the line which connects them. The number of times, n_s, this is performed thus provides an estimate of the Lyapunov exponent, λ_n, along the reference trajectory (Neufeld & Tél 1998). We note that the spatial distribution of λ_n is highly varied, being positive in the mixing region but vanishing in the regular region within the vortex core (Babiano *et al.* 1994; Neufeld & Tél 1998). Using a large number of randomly selected reference trajectories (not taking into consideration those which are permanently trapped by the vortex cores), the largest values of λ_n for the symmetrical and skew-symmetrical channels are obtained as 0.084 and 0.085 respectively. Using (8.3), the fractal dimensions of the symmetrical and skew-symmetrical channels are thus calculated as 1.63 and 1.65, which are in good agreement with the values obtained from figure 27. We may thus conclude that hyperbolicity plays a crucial role in the dynamics of the present problem outside the stable region, where almost all initial conditions lead to orbits that eventually escape the mixing region at exponential rate. The vortex core, nonetheless, gives rise to non-hyperbolicity and is characterized by space-filling fractality ($D_0 = 2$) (e.g. Lau, Finn & Ott 1991; Motter, Lai & Grebogi 2003; de Moura & Grebogi 2004).

9. Conclusions

We have considered open flow in channels where the mixing process is induced primarily by unsteady motion of point vortices located in the trough region of the wavy wall. Assuming two-dimensional irrotational, incompressible flow, the equations of motion for the vortices and the particles have been derived. Their instantaneous positions have been tracked using the Lagrangian technique and have been conformally mapped to the physical domain. Perturbation analysis indicates that the frequency of vortex motion is weakly dependent on the wall amplitude but that a characteristic Strouhal number $\omega/UK \sim 0.25$ occurs for a wide range of input parameters. The analytical and numerical vortex paths agree well for small perturbation. It has been found that the vortex trajectory is governed mainly by its image, with little effect arising from the presence of neighbouring vortices along the wavy wall or channel.

Particle trajectories and snapshots have revealed the stretching and folding processes and increasing scattering that characterize chaotic motion. Particles seeded within the

separation bubble have been found to escape from the trough (hence the vortex), primarily during the first oscillation cycle. A major fraction of particles retained is made up of those seeded at close proximity to the singular point, a stable region which constitutes a 'core' surrounding and shielding the vortex singularity. Significant mass exchange takes place between particles inside and outside the separation bubble, forming a chaotic-sea-of-mixing region which evolves in size as the vortex moves. The dynamics are in good qualitative agreement with previously reported solutions of the unsteady Navier–Stokes equations for a wavy channel with oscillatory unidirectional flow.

Statistical evaluation of the particle positions has shown that the skew-symmetrical wavy channel is more efficient in passive mixing than a symmetrical wavy channel. Incorporating the effect of diffusion via gridless random walk increases lateral particle dispersion significantly despite a marked reduction in the standard deviation of the longitudinal particle positions.

Using the non-escaping vortex core as a source of reacting particles, we have considered autocatalytic reaction in the wavy channel and verified that the unstable manifold acts as an effective catalyst for the process. Fractal enhancement of productivity ($D_0 \approx 1.65$) has been identified. The symmetrical wavy channel shows augmentation of area covered by B particles at high reaction rates due to infection of the vortices at the opposite wall. The fractal dimensions obtained correlate well to the escape rates and the Lyapunov exponents if only the hyperbolic dynamics is considered. Non-hyperbolicity is present but is confined to the stable region within the vortex core.

The simplicity of the present model and its qualitative accuracy make it attractive for the study of a wide range of vortex-induced transport and mixing problems in channels with wavy or zigzag configurations.

The authors are very grateful to György Károlyi of Budapest University of Technology and Economics for his helpful comments on a previous draft. We would also like to thank the reviewers of earlier versions of this manuscript for their constructive criticism. The first author acknowledges the scholarship awarded by Universiti Teknologi MARA and the Malaysian Ministry of Higher Education. Part of the computation has been carried out using resources provided by the Oxford Supercomputing Centre.

REFERENCES

Amon, C. H., Guzmán, A. M. & Morel, B. 1996 Lagrangian chaos, Eulerian chaos, and mixing enhancement in converging-diverging channel flows. *Phys. Fluids* **8** (5), 1192–1206.

Aref, H. 1984 Stirring by chaotic advection. *J. Fluid Mech.* **143**, 1–21.

Babiano, A., Boffetta, G., Provenzale, A. & Vulpiani, A. 1994 Chaotic advection in point vortex models and two-dimensional turbulence. *Phys. Fluids* **6** (7), 2465–2474.

Biemond, J. J. B., De Moura, A. P. S., Károlyi, G., Grebogi, C. & Nijmeijer, H. 2008 Onset of chaotic advection in open flows. *Phys. Rev.* E **78** (1), 016317

Boffetta, G., Celani, A. & Franzese, P. 1996 Trapping of passive tracers in a point vortex system. *J. Phys.* A **29** (14), 3749–3759.

Borthwick, A. G. L. & Barber, R. W. 1992 Numerical simulation of jet-forced flow in a circular reservoir using discrete and random vortex methods. *Intl J. Numer. Methods Fluids* **14** (12), 1453–1472.

Budyansky, M., Uleysky, M. & Prants, S. 2004 Hamiltonian fractals and chaotic scattering of passive particles by a topographical vortex and an alternating current. *Physica* D **195** (3–4), 369–378.

Budyansky, M. V., Uleysky, M. Y. & Prants, S. V. 2007 Lagrangian coherent structures, transport and chaotic mixing in simple kinematic ocean models. *Commun. Nonlinear Sci. Numer. Simul.* **12** (1), 31–44.

Cadwell, L. H. 1994 Singing corrugated pipes revisited. *Am. J. Phys.* **62** (3), 224–227.

Chorin, A. J. 1973 Numerical study of slightly viscous flow. *J. Fluid Mech.* **57**, 785–796.

Crawford, F. S. 1974 Singing corrugated pipes. *Am. J. Phys.* **42** (4), 278–288.

Csanady, G. T. 2001 Drag generation mechanisms. In *Wind Stress Over the Ocean* (ed. I. S. F. Jones & Y. Toba), pp. 124–141. Cambridge University Press.

Cannell, P. & Ffowcs Williams, J. E. 1973 Radiation from line vortex filaments exhausting from a two-dimensional semi-infinite duct. *J. Fluid Mech.* **58** (1), 65–80.

Guzmán, A. M. & Amon, C. H. 1994 Transition to chaos in converging-diverging channel flows: Ruelle–Takens–Newhouse scenario. *Phys. Fluids* **6** (6), 1994–2002.

Guzmán, A. M. & Amon, C. H. 1996 Dynamical flow characterization of transitional and chaotic regimes in converging-diverging channels. *J. Fluid Mech.* **321**, 25–57.

Howe, M. S. 2003 *Theory of Vortex Sound*. Cambridge University Press.

Károlyi, G., Péntek, Á., Toroczkai, Z., Tél, T. & Grebogi, C. 1999 Chemical or biological activity in open chaotic flows. *Phys. Rev.* E **59** (5), 5468–5481.

Károlyi, G. & Tél, T. 2007 Effective dimensions and chemical reactions in fluid flows. *Phys. Rev.* E **76** (4), 046315.

Lamb, H. 1953 *Hydrodynamics*, 6th edn. Cambridge University Press.

Landau, L. D. & Lifshitz, E. M. 1987 *Fluid Mechanics*, 2nd edn. Pergamon.

Lau, Y.-T., Finn, J. M. & Ott, E. 1991 Fractal dimension in nonhyperbolic chaotic scattering. *Phys. Rev. Lett.* **66** (8), 978–981.

Liang, Q., Taylor, P. H. & Borthwick, A. G. L. 2007 Particle mixing and reactive front motion in unsteady open shallow flow – modelled using singular value decomposition. *Comput. Fluids* **36** (2), 248–258.

Metcalfe, G. & Ottino, J. M. 1994 Autocatalytic processes in mixing flows. *Phys. Rev. Lett.* **72** (18), 2875–2880.

Milne-Thomson, L. M. 1968 *Theoretical Hydrodynamics*, 5th edn (revised). Macmillan.

Motter, A. E., Lai, Y.-C. & Grebogi, C. 2003 Reactive dynamics of inertial particles in nonhyperbolic chaotic flows. *Phys. Rev.* E **68**, 056307.

de Moura, A. P. S. & Grebogi, C. 2004 Reactions in flows with nonhyperbolic dynamics. *Phys. Rev.* E **70**, 036216.

Nayfeh, A. H. 1985 *Problems in Perturbation*. John Wiley.

Neufeld, Z. & Tél, T. 1997 The vortex dynamics analogue of the restricted three-body problem: advection in the field of three identical point vortices. *J. Phys.* A **30** (6), 2263–2280.

Neufeld, Z. & Tél, T. 1998 Advection in chaotically time-dependent open flows. *Phys. Rev.* E **57** (3 Suppl. A), 2832–2842.

Nishimura, T. & Matsune, S. 1996 Mass transfer enhancement in a sinusoidal wavy channel for pulsatile flow. *Heat Mass Transfer* **32** (1–2), 65–72.

Ottino, J. M. 1989 *The Kinematics of Mixing: Stretching, Chaos and Transport*. Cambridge University Press.

Pentek, A., Karolyi, G., Scheuring, I., Tel, T., Toroczkai, Z., Kadtke, J. & Grebogi, C. 1999 Fractality, chaos and reactions in imperfectly mixed open hydrodynamical flows. *Physica* A **274** (1), 120–131.

Ralph, M. E. 1986 Oscillatory flows in wavy-walled tubes. *J. Fluid Mech.* **168**, 515–540.

Roberts, E. P. L. & Mackley, M. R. 1996 The development of asymmetry and period doubling for oscillatory flow in baffled channels. *J. Fluid Mech.* **328**, 19–48.

Rom-Kedar, V., Leonard, A. & Wiggins, S. 1990 Analytical study of transport, mixing and chaos in an unsteady vortical flow. *J. Fluid Mech.* **214**, 347–394.

Rom-Kedar, V. & Wiggins, S. 1990 Transport in two-dimensional maps. *Arch. Ration. Mech. Anal.* **109** (3), 239–298.

Routh, E. J. 1881 Some applications of conjugate functions. *Proc. Lond. Math. Soc.* **s1–12**, 73–89.

Silverman, M. P. & Cushman, G. M. 1989 Voice of the dragon: the rotating corrugated resonator. *Eur. J. Phys.* **10**, 298–304.

Sobey, I. J. 1980 On flow through furrowed channels. Part 1. Calculated flow patterns. *J. Fluid Mech.* **96** (1), 1–26.

Sobey, I. J. 1982 Oscillatory flows at intermediate Strouhal number in asymmetric channels. *J. Fluid Mech.* **125**, 359–373.

Sobey, I. J. 1985 Dispersion caused by separation during oscillatory flow through a furrowed channel. *Chem. Engng Sci.* **40** (11), 2129–2134.

Stephanoff, K. D., Sobey, I. J. & Bellhouse, B. J. 1980 On flow through furrowed channels. Part 2. Observed flow patterns. *J. Fluid Mech.* **96** (1), 27–32.

Taylor, P. H. 1981 Flow excited motion of some unusual surfaces. PhD thesis, University of Cambridge, Cambridge, UK.

Tél, T. & Gruiz, M. 2006 *Chaotic Dynamics: An Introduction Based on Classical Mechanics*. Cambridge University Press.

Tél, T., de Moura, A., Grebogi, C. & Károlyi, G. 2005 Chemical and biological activity in open flows: a dynamical system approach. *Phys. Rep.* **413**, 91–196.

Toroczkai, Z., Károlyi, G., Péntek, Á., Tél, T. & Grebogi, C. 1998 Advection of active particles in open chaotic flows. *Phys. Rev. Lett.* **80** (3), 500–503.

Walker, J. 2007 *The Flying Circus of Physics*. John Wiley.

Wierschem, A. & Aksel, N. 2004 Influence of inertia on eddies created in films creeping over strongly undulated substrates. *Phys. Fluids* **16** (12), 4566–4574.

Wierschem, A., Scholle, M. & Aksel, N. 2003 Vortices in film flow over strongly undulated bottom profiles at low Reynolds numbers. *Phys. Fluids* **15** (2), 426–435.

Wilson, M. C. T., Summers, J. L., Kapur, N. & Gaskell, P. H. 2006 Stirring and transport enhancement in a continuously modulated free-surface flow. *J. Fluid Mech.* **565**, 319–351.